JGR Solid Earth

RESEARCH ARTICLE
10.1029/2022JB024598

Key Points:

- A new receiver function method is developed to estimate dip direction, depth, and thickness of a dipping layer
- Applying this method to the Sumatran subduction zone, we identify dipping low-velocity layers along slab interface
- The dipping layer with abnormal thickness and dip direction is interpreted as a hydrated and diffused plate boundary

Supporting Information:

Supporting Information may be found in the online version of this article.

Correspondence to:

L. Chen and S. Wei,
lchen@mail.iggcas.ac.cn;
shjwei@ntu.edu.sg

Citation:

Feng, M., Chen, L., Wei, S., Wang, X., Wang, X., & Wu, Z. (2023). A new method to estimate slab dip direction using receiver functions and its application in revealing slab geometry and a diffuse plate boundary beneath Sumatra. *Journal of Geophysical Research: Solid Earth*, *128*, e2022JB024598. https://doi.org/10.1029/2022JB024598

Received 14 APR 2022
Accepted 16 MAR 2023

Author Contributions:

Conceptualization: Mingye Feng, Ling Chen, Shengji Wei
Data curation: Ling Chen, Shengji Wei, Xin Wang
Formal analysis: Mingye Feng, Ling Chen, Shengji Wei, Xin Wang
Funding acquisition: Ling Chen, Shengji Wei
Investigation: Mingye Feng, Ling Chen, Shengji Wei, Xin Wang, Xu Wang
Methodology: Mingye Feng, Ling Chen, Shengji Wei, Xin Wang
Project Administration: Ling Chen, Shengji Wei
Resources: Mingye Feng, Ling Chen, Shengji Wei, Xin Wang
Software: Mingye Feng, Xin Wang

A New Method to Estimate Slab Dip Direction Using Receiver Functions and Its Application in Revealing Slab Geometry and a Diffuse Plate Boundary Beneath Sumatra

Mingye Feng[1,2,3,4], Ling Chen[1,2], Shengji Wei[3,4], Xin Wang[5], Xu Wang[1], and Zimu Wu[1,2]

[1]State Key Laboratory of Lithospheric Evolution, Institute of Geology and Geophysics, Chinese Academy of Sciences, Beijing, China, [2]College of Earth and Planetary Sciences, University of Chinese Academy of Sciences, Beijing, China, [3]Earth Observatory of Singapore, Nanyang Technological University, Singapore, Singapore, [4]Asian School of the Environment, Nanyang Technological University, Singapore, Singapore, [5]Key Laboratory of Earth and Planetary Physics, Institute of Geology and Geophysics, Chinese Academy of Sciences, Beijing, China

Abstract While dip direction is a fundamental parameter of slab geometry, it is rarely estimated quantitatively. Here, we develop a new method, Dip Direction Searching (DDS), of receiver functions (RFs) that reduces the uncertainty of slab dip direction estimation from tens to several degrees. DDS can also resolve the thickness and depth of a dipping structure. We then apply DDS to the RFs in the Sumatran subduction zone. Travel time differences of the converted phases from the upper and lower (oceanic Moho) boundaries of the dipping low-velocity layer (LVL) along the plate interface show a thickness of 10–14 km. The results also show increased dip direction of the slab Moho from 47 ± 5.3° in southern Sumatra to 70 ± 10.7° in northern Sumatra, indicating a complicated slab geometry and internal deformation along strike. Similar dip directions are obtained for the upper and lower LVL boundaries beneath Nias and Enggano forearc islands in the north and south, whereas we find a larger discrepancy of ∼14–23° beneath Siberut and Pagai in between. The thicker LVL with a non-negligible difference in the dip directions of its upper and lower bounds in the center of Sumatra is interpreted as a partially serpentinized mantle layer above the oceanic crust, forming a distinct channel atop the subducting slab. Our results provide basic observational constraints on the structure and geometry of the oceanic slab and associated subduction processes. Both synthetics and data analyses also indicate DDS can be applied in other subduction zones and for other dipping interfaces.

Plain Language Summary Subducting plate boundary, between the oceanic and the continental plates, is key to understanding material and energy exchanges in the subduction factory and the associated geohazards. Seismic imaging reveals a dipping low-velocity layer (LVL) at the subducting plate boundary globally associated with megathrust earthquakes and arc magmatism, but the nature of the LVL remains hotly debated because of lacking strong constraints on its geometry and properties and regional comparisons. To partly fill the knowledge gap, we propose a Dip Direction Searching (DDS) method to detect the LVL, estimate the dip directions of its upper and lower boundaries, and constrain its depths and thickness based on seismic P-wave to S-wave converted phases. DDS is then applied to the Sumatra subduction zone as a case study, and an LVL is successfully detected with a large thickness (up to 14 km) than a normal oceanic crust (∼7 km). The dip directions of the upper and lower boundaries of the LVL differ by up to 23°, suggesting a considerably irregular upper boundary. We interpret the LVL as the oceanic crust overlain by a low-velocity hydrated mantle layer, indicating a smeared/diffuse plate boundary caused by upward fluid migration and its resultant mantle serpentinization.

1. Introduction

Slab geometry, depicted by the geometries of slab boundaries and interfaces, is of great significance in understanding the geodynamic processes of subduction (Zhao et al., 2017). The geometry of slab-related discontinuities, such as the boundaries between the descending slab and surrounding mantle (e.g., slab top surface) and the slab Moho (Kawakatsu & Watada, 2007; Kim et al., 2021), is defined by the dip angle and dip direction. The geometry of the slab-related discontinuities could be complicated due to internal slab deformation and lateral variations of slab properties, such as in the Japan and Sumatra-Java subduction zones, where both the dip angle and dip direction of the slab vary laterally (e.g., Hall & Spakman, 2015; Singh, Hananto, Mukti, et al., 2011; Zhao

Supervision: Ling Chen, Shengji Wei, Xin Wang
Validation: Mingye Feng, Ling Chen, Shengji Wei, Xin Wang
Writing – original draft: Mingye Feng
Writing – review & editing: Mingye Feng, Ling Chen, Shengji Wei, Xin Wang, Xu Wang, Zimu Wu

et al., 2017). To understand the subduction processes and related slab deformation, a large variety of seismological methods have been proposed to explore slab layering and slab geometric parameters (e.g., Chen et al., 2005; Singh et al., 2012; Zhao et al., 2017).

Geometries and layering of slabs are often determined using active-source seismic survey, passive-source seismic tomography and discontinuity imaging, or slab contour models. Active-source imaging has the highest resolution but is rather expensive. Moreover, active source surveys cover a limited number of locations, and the detection depth is limited to less than 40 km generally (e.g., Mukti et al., 2012; Tang et al., 2013). Passive-source seismic tomography can image the morphology and geometry of downgoing slabs as velocity anomalies down to a depth of thousands of kilometers. However, due to limited source and receiver configuration, the tomography resolution (e.g., >50 km) is usually insufficient to determine the position and geometry of slab boundaries precisely (e.g., Zhao et al., 2017, 2021). Slab contour model, mainly based on seismicity, is an alternative way to estimate slab dip direction (Audet et al., 2010; Gosselin et al., 2020), such as the Slab2 model (Hayes et al., 2018). The Slab2 model constrains the average morphology and geometry of a slab top surface based on active source seismic data interpretations, receiver functions (RFs), local/regional and global seismicity catalogs, and seismic tomography models (Hayes et al., 2018). However, the Slab2 model describes only the upper boundary of slab with no constraints on slab layering and has large uncertainties in areas with poor data coverage. Because the data coverage is highly uneven globally, the precision and resolution of the model results are much different among subduction zones, which hinders detailed regional comparisons.

RF is a time series of structural responses (Ammon, 1991) that can be used to effectively image slab-related discontinuities beneath seismic stations such as the Moho and slab boundaries (Bostock, 2013; Chen et al., 2005; Kawakatsu & Watada, 2007; X. Li et al., 2000; Shiomi et al., 2004; Tonegawa et al., 2006; Yuan et al., 2000). Although previous studies have proposed various RF imaging methods to constrain the slab dip angle, far less effort has been made to estimate the slab dip direction in detail (e.g., Chen et al., 2005; Cheng et al., 2017; Schneider et al., 2013; Tauzin et al., 2016). Some previous RF studies focus on using transverse receiver functions (T-RFs) to reveal dipping and/or anisotropic structures beneath a station based on the polarity reversal of the P-to-S (Ps) and the zero-lag phases in back azimuth (e.g., Cassidy, 1992; Hayes & Furlong, 2007; Porter et al., 2011; Savage, 1998). However, T-RFs are easier to be contaminated by noise than the radial receiver functions (R-RFs) due to weaker amplitudes, especially in the case of near-flat interfaces or weak anisotropic layers; thus, the back azimuthal variation is not easy to trace to locate polarity changes. To increase the signal-to-noise ratio, back azimuthal binning (e.g., ∼5–10°) is commonly used, inevitably reducing the resolution of dip direction estimation. Besides, the polarity analysis on T-RFs will fail with insufficient back azimuthal coverage around the strike direction of dipping interface (Audet et al., 2010) or with the presence of strong anisotropy that perturbs the back azimuthal variation in both polarity and arrival time. To separate the respective signals of isotropic and anisotropic structures (including dipping structures) that govern the back azimuthal variations, a harmonic decomposition method is proposed, which divides the back azimuthal variation of amplitude into orthogonal harmonic components in a set of orders (Bianchi et al., 2010; Piana Agostinetti & Miller, 2014; Shiomi & Park, 2008). This method can estimate the orientations of symmetric axes within anisotropic crustal layers and can also be applied to estimate the dip direction of dipping layers (Audet, 2015; Schulte-Pelkum & Mahan, 2014). Recently, Zhang et al. (2019) introduced a data-driven method, in which principal component analysis (PCA) is adopted to decompose RFs by principal eigenvalues, and apply it to estimate the dip direction of the Moho discontinuity.

In this study, we propose to constrain the slab dip direction by a new method, Dip Direction Searching (DDS), which is a grid-search scheme to fit the two-lobed harmonic back azimuthal variation of Ps conversions primarily in the R-RFs (Figure 1). Such a grid-search method works well in constraining the trend of the symmetric axis of the structure in an anisotropic crust (e.g., Liu & Niu, 2012; Wu et al., 2019). As a case study, we apply the DDS method to the Sumatran subduction zone, where the seismic networks are sparse. This application is designed to (a) examine the ability of DDS using sparse seismic data, to provide structural and geometric constraints for slab interfaces; (b) showcase the significance of DDS results in understanding slab deformation and dehydration processes at the subducting plate boundary.

In the rest of the paper, we first present the details of the DDS method, and then validate the method with a series of synthetic tests. We also compare our DDS estimation with that derived from the PCA (Zhang et al., 2019) for benchmarking and performance evaluation. We then apply the DDS method, complemented by PCA and T-RF analysis, to the Sumatran subduction zone to derive the geometry and layering structure of the subducting slab.

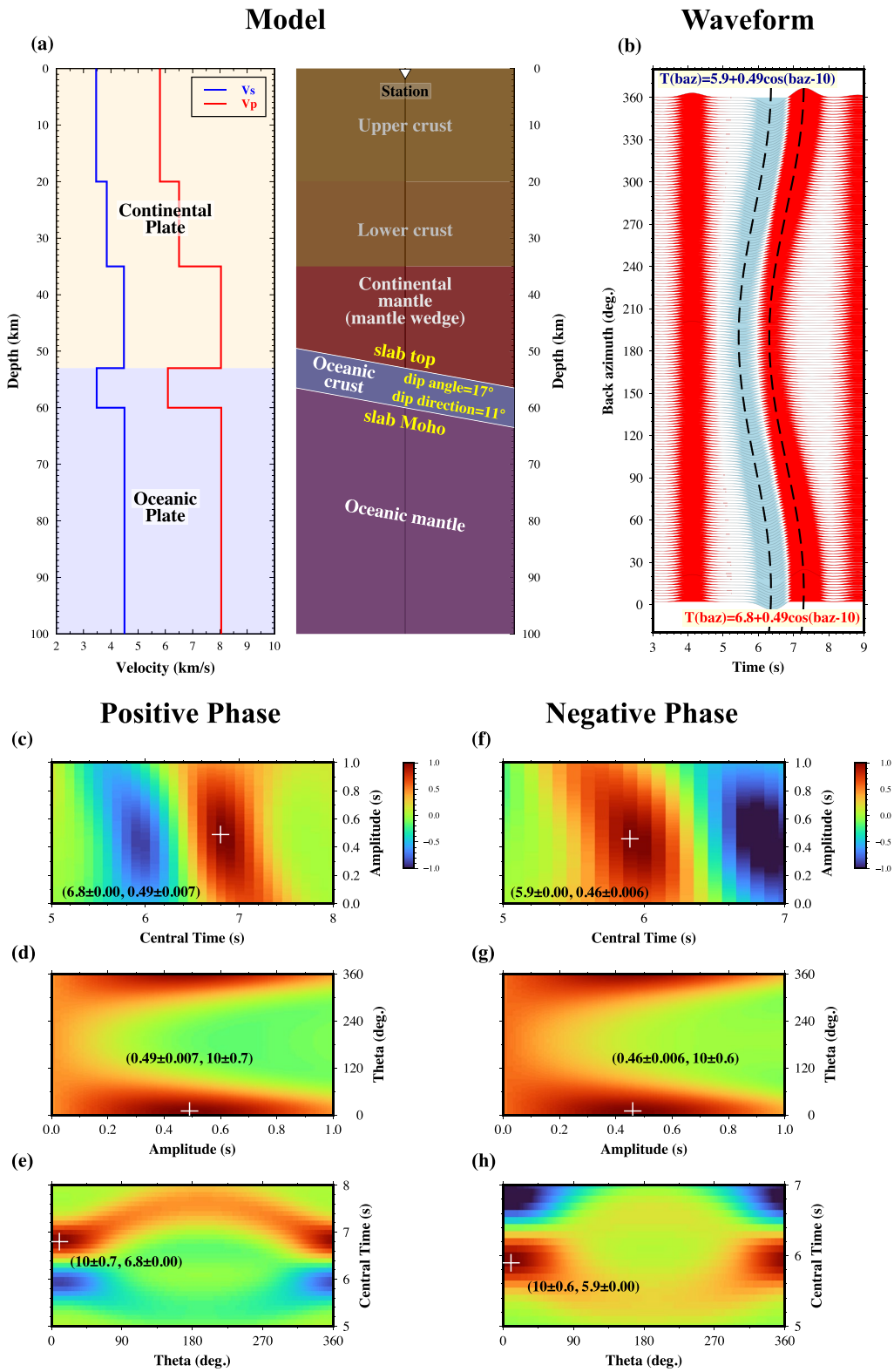

Figure 1.

This is followed by our interpretations on the variation of slab dip direction and the dipping layer structure. Finally, we discuss the generalization and potential improvements of DDS.

2. Methods

2.1. Synthetic RF Calculation

We calculate synthetic seismic waveforms by the RAYSUM code, which is a ray-based code to calculate the traveltime and amplitude of specific seismic phases and compose synthetic seismograms for anisotropic media and dipping discontinuities (Frederiksen & Bostock, 2000). We allow the code to generate multiples from all discontinuities. The RFs are generated by a time-domain iterative deconvolution method (Kikuchi & Kanamori, 1992; Ligorría & Ammon, 1999) with a low-pass Gaussian filter. Gaussian filtering coefficients are set to be 1.5 and 2.5, corresponding to the upper corner frequencies of ∼0.5 and ∼0.8 Hz, respectively (where the amplitude of Gaussian function drops by a factor of e in the frequency domain).

2.2. Dip Direction Searching

Theoretical studies and observations indicate that the RF Ps conversions vary with back azimuth, and approximately accord with a harmonic function (i.e., sinusoidal functions) for a gently dipping velocity interface or a weak anisotropic structure above the interface (Cassidy, 1992; Levin & Park, 1997; J. Li et al., 2019; Savage, 1998; P. Wang et al., 2010). Regardless of the anisotropic effect, the back azimuthal variation induced by a dipping interface exhibits a period of 2π (Figure S1 in Supporting Information S1). Thus, we can use a cosine function to fit the back azimuthal variation of Ps arrival times as shown in Equation 1 (Cassidy, 1992; J. Li et al., 2019).

$$T(\alpha) = T_0 + A\cos(\alpha - \theta), \tag{1}$$

where α denotes back azimuth, and θ indicates the dip direction; T_0 is called central time, which is the arrival time of Ps phase relative to direct P-wave coming along the strike of the interface; A is the amplitude of the cosine function, which depends on the dip angle and velocity structure (J. Li et al., 2019; Rossi et al., 2006; Tan et al., 2018). For anisotropic medium, the Ps arrival time T varies relative to back azimuth with a period of π to 2π (Cassidy, 1992; Levin & Park, 1997; J. Li et al., 2019; Savage, 1998; Zhang et al., 2019). The period and phase of the high-order terms are associated with the plunging angle and the trend of the symmetric axis of the overlying anisotropic material (J. Li et al., 2019; Zhang et al., 2019). Thus, the parameterization of anisotropy is difficult without the knowledge of the anisotropic type, such as the symmetric axes of the overriding materials (J. Li et al., 2019). Using high-order terms in fitting azimuthal variation of Ps phase is generally subjected to over-fitting, in particular when the noise level is high, and the multiples generated from intra-crustal interfaces are strong. Here, we consider only the first-order term, as shown by Equation 1, to simplify the problem, and enhance the stability according to Occam's Razor. As will be demonstrated by the synthetic tests in Section 3, the structure with anisotropy amplitude less than ∼5%–10%, has a negligible influence on the accuracy of DDS even in the case of complicated combinations of anisotropic layers.

We use a grid search strategy to find the optimal solution of the three parameters (T_0, A, and θ) (Julià, 2007; J. Li et al., 2019; Rost & Thomas, 2002; Zhu & Kanamori, 2000). We name this method as DDS. During our grid search, θ varies from 0° to 360° with an interval of 1°, A ranges from 0 s to 1.0–2.0 s at an interval of 0.01 s, and central time of the target phase (T_0) changes with an interval of 0.1 s. Search limits for A and T_0 are first roughly determined by visual inspection and then refined by trial and error. We stack the amplitude of RFs at the arrival time calculated from Equation 1 for all possible combinations of the three parameters. For a negative amplitude target phase, we reverse the polarity before stacking. The normalized stacking amplitude is regarded as the energy of certain combination of the three parameters. The maximum of the normalized stacking energy (i.e., 1) corresponds to the optimal combination of the three parameters, which optimally fits the back azimuthal

Figure 1. Model 0 and the reproduced dip direction estimates by Dip Direction Searching (DDS). (a) The velocity model and layered structure. (b) The synthetic receiver function (RF) waveforms. The highlighted positive-negative pulse doublet by the dashed line indicates Ps phases converted from slab Moho and slab upper boundary (slab top), respectively, as noted in (a). The dashed lines are the optimal cosine functions to fit their back azimuthal variations, with their expressions labeled in the same color. Figures (c)–(e) are transects through the T_0-A-θ search "cube" for the positive Ps phase at the optimal point. Figures (f)–(h) are similar to (c)–(e) but for the negative phase.

variation (Figures 1c, and 1h and Figure S1b in Supporting Information S1). Note, the RF waveforms before stacking in back azimuth are used as the input for DDS. Here, we evaluate the uncertainty of each parameter by a bootstrapping method (Efron & Tibshirani, 1986). One hundred bootstrap iterations are used. For every bootstrap subset, we randomly sample the same volume of RFs from the original data set with replacement. The resampling percentage is generally 60%–70%, about 63% on average.

Since the incident angles of teleseismic waves at receivers differ with epicenter distance, a moveout correction is required to mitigate the impact of epicenter distance difference on the variation of arrival times before grid search. In general, a global average velocity model is sufficient for this purpose (J. Li et al., 2019). Here, we conduct moveout correction to real RF waveforms using a ray parameter of 0.065 s/km based on the IASP91 global velocity model (Kennett & Engdahl, 1991). This horizontal layer assumption has insignificant influence on DDS estimation at least when dip angle is <30° (Figure S2 in Supporting Information S1).

2.3. Principal Component Analysis

In addition to the harmonic back azimuthal variation, the dip direction can be indicated by the reconstructed RFs with principal features through PCA on RFs (Figures S1d–S1f in Supporting Information S1; Zhang et al., 2019). Following Zhang et al. (2019), we stack the R-RFs within 10° of back azimuth after moveout correction. Then, we extract the three largest eigenvalues from the RF covariance matrix to retrieve the decomposed R-RF waveforms, which correspond to the principal components (PCs). The first-PC reconstruction of RFs shows the primary feature of original P-RFs, reflecting the average structural information. The second-PC reconstruction indicates the structural variation reflected in original P-RFs. In the second-PC reconstruction, the back azimuth corresponding to the polarity flipping of the targeting phase defines the strike direction of the dipping interface, and the dip direction is strike plus or minus 90° (Figure S1 in Supporting Information S1). Basic principle and workflow of PCA are stated in Text S1 in Supporting Information S1.

2.4. Transverse Receiver Function Analysis

For a dipping interface, the travel time pattern in T-RFs is similar to that in R-RFs, but the polarity of phases (both the Ps and zero-lag phases) flips across the dip direction (Figure S1c in Supporting Information S1). Therefore, we can use the polarity flipping of the zero-lag phase and the cosine azimuthal variation of the Ps phase in T-RFs to verify the DDS results from R-RFs (Figure S1c in Supporting Information S1). We name this procedure as transverse receiver function analysis (TRFA), which supplies auxiliary dip direction estimations.

3. Synthetic Testing

3.1. Model Setup

To validate our new method, we compare the performance of DDS against PCA through various synthetic tests. To generate the synthetics, we modify the AK135 model (Kennett et al., 1995) to add a subducted oceanic crust at the depth around 50 km (Figure 1a). To mimic the Sumatran subduction zone, as shown in the Slab2 model, the dip direction and the dip angle of the subducting slab are set to 11° and 17°, respectively. The depth of the upper slab boundary (slab top) is set to 53 km and the depth of slab Moho to 60 km, imitating the slab depth at the Sumatran forearc area (Singh, Hananto, Mukti, et al., 2011; Singh et al., 2012). We set the subducting slab velocity model to the values extracted from the Crust1.0 model in the Indian Ocean (Laske et al., 2012).

3.2. Robustness Tests

This reference velocity model is firstly used to generate synthetic RFs for a simple scenario (Model 0). Figure 1b shows a pair of negative and positive signals, with their arrival times varying as a function of back azimuth. These signals are the Ps phases from the slab top and slab Moho, respectively. We applied our DDS method to these synthetic data and obtained the dip direction of $10 \pm 0.7°$ and strike direction of $280 \pm 0.7°$, highly consistent with the input model (Figure 1).

Considering the complexity of real RF waveforms, we then conduct a series of additional synthetic tests to further examine the performance of the DDS method. These tests include 22 scenarios to cover incomplete back

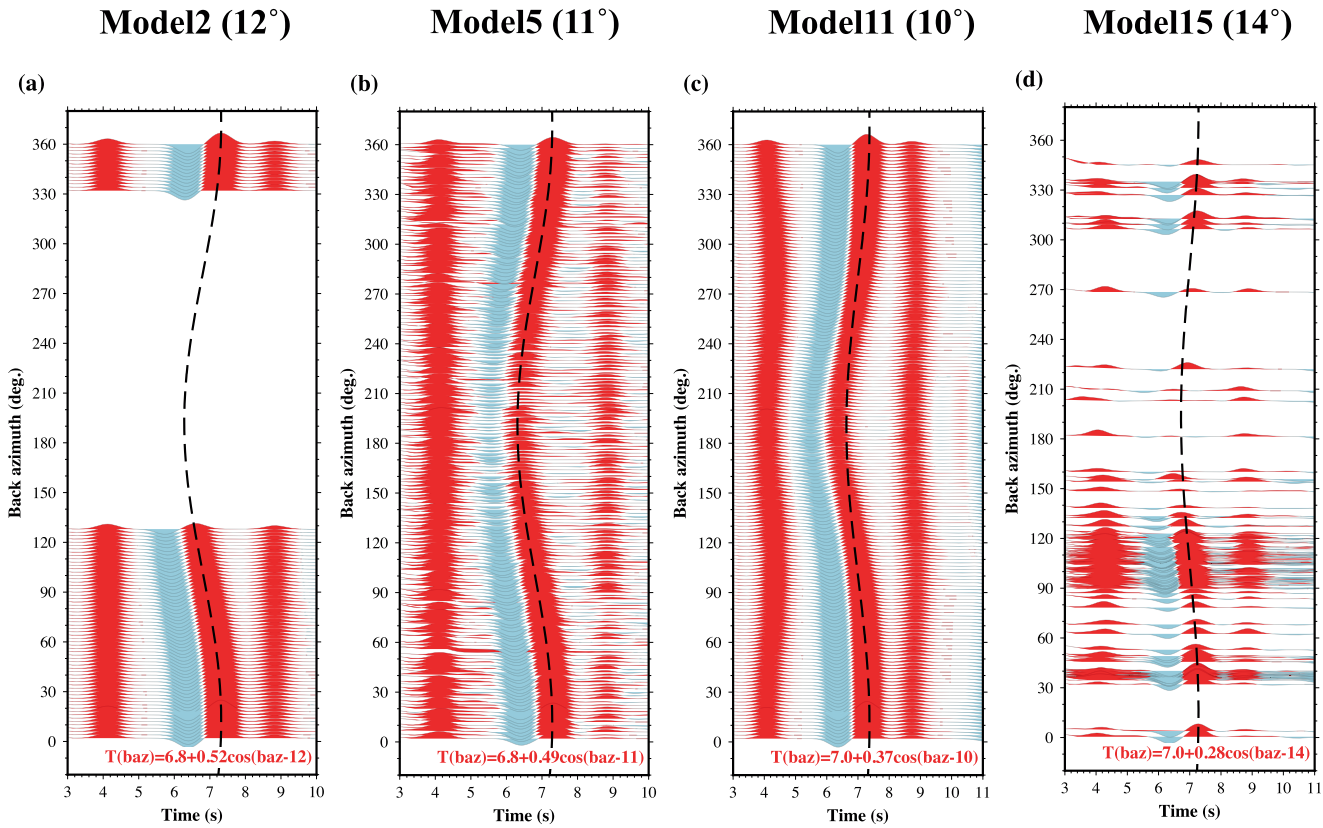

Figure 2. Synthetic receiver functions (RFs) of Models 2, 5, 11, and 15 and their dip direction estimates. (a) In Model 2, we delete the traces in the 130°–330° back azimuthal range; (b) in Model 5, we add 25% strength of white noise; (c) Model 11 includes a 2% anisotropic crust and a 0.3% anisotropic mantle wedge; (d) Model 15 features the compound effects of uneven and incomplete back azimuthal distribution (as in Model 3), anisotropic structure (as in Model 11), and 25% strength of white noise (as in Model 5).

azimuthal coverage, high noise level, crustal and mantle anisotropy, and their compound effects. The details of 22 input models (Models 1–15 and S1–S7) are described in Texts S2 and S3 in Supporting Information S1, with the corresponding results shown in Table 1 and Table S1 in Supporting Information S1. For most cases, dip directions are accurately estimated with deviation ≤3° from the input. These tests demonstrate that DDS is applicable with high accuracy to the data set where the back azimuthal coverage is incomplete, even with a ∼180° azimuthal gap (Figure 2a; Model 2). Such high accuracy is also achievable for the data set that has a noise level at the strength of 25% of the signal (Figure 2b; Model 5). The largest deviations of 11–12° are associated with Models 7 and S4. Model 7 is characterized by an anisotropic mantle wedge with a strength of 10% and a near trench-perpendicular symmetric axis (Figure S3 in Supporting Information S1), and Model S4 has an anisotropic lower crust with a strength of 5% and a trench-parallel 30°-dipping symmetric axis. For the other models with anisotropy, the deviation is ≤6° and mostly ≤3°. In these anisotropy tests, the accuracy is governed by both anisotropy strength and the orientation of the symmetric axis. Accurate DDS estimation can be obtained with presence of 5%–10% anisotropy in the mantle wedge and 2%–5% of anisotropy in the crust (e.g., Model 11; Figure 2c). For the case with very high degree of anisotropy in upper and lower crust (e.g., 10%; Models S2 and S5), the target phases would be significantly affected thus DDS becomes inapplicable (Figure S4 in Supporting Information S1). But the case could be excluded by visual inspection to avoid biased estimation.

We then apply a complicated real anisotropy model obtained from RF modeling in Japan subduction zone (Wirth & Long, 2012) to test DDS (Text S2 in Supporting Information S1). The retrieved dip direction shows only 1° deviation relative to the input (Figure S5 in Supporting Information S1), suggesting broad applicability of DDS. Apart from the individual effects of anisotropy, back azimuthal coverage, and noise level, we also demonstrate that their compound effects bias DDS estimation insignificantly even when taking realistic back azimuthal cover-

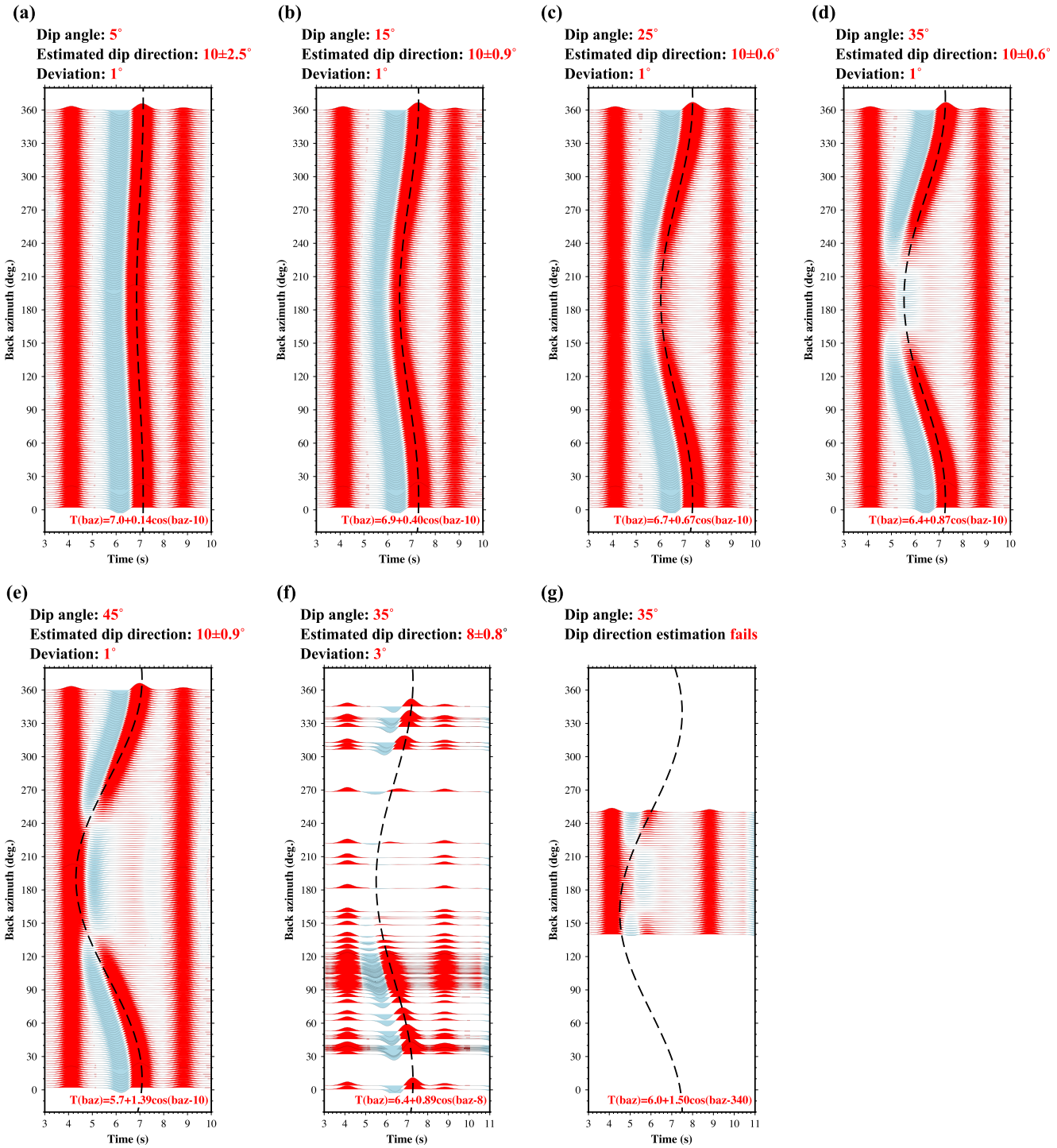

Figure 3. The impact of varying dip angle on Dip Direction Searching (DDS) estimation. Figures (a)–(e) show the synthetic waveforms and DDS estimates of Model 0 with the dip angle changing from 5° to 45°. Figures (f)–(g) show the DDS estimation for the cases of 35° dip angle. In (f), receiver functions (RFs) are unevenly distributed in back azimuth. In (g), RFs are distributed only at the back azimuths between 140° and 250°, which leads to a possibly failed DDS estimation.

age into consideration (e.g., Model 15; Figure 2d). We also test the performance of DDS for different dip angles of the slab. With the dip angle varying from 5° to 45° even with some uneven back azimuthal sampling, the deviations are ≤3° (Figure 3). From all these synthetic tests, we show high robustness of DDS and its promising application to real data.

Table 1
The Dip Direction Parameters Derived by DDS and PCA for the Synthetic Models[a]

	DDS estimation				PCA estimation[b,c]	
Model[e]	Dip direction (°)	Deviation from input (°)	Central time (s)	Amplitude (s)	DD-1 (±5°)	DD-2 (±5°)
Model 0	10 ± 0.7	1	6.8 ± 0.00	0.49 ± 0.007	10–20	0–10
Model 1	8 ± 1.2	3	6.8 ± 0.00	0.49 ± 0.012	10–20	0–10
Model 2	12 ± 0.3	1	6.8 ± 0.00	0.52 ± 0.012	/[d]	330–340
Model 3	13 ± 4.0	2	6.8 ± 0.03	0.50 ± 0.024	0–40	350–360
Model 4	10 ± 0.7	1	6.8 ± 0.00	0.49 ± 0.007	10–20	0–10
Model 5	11 ± 0.8	0	6.8 ± 0.00	0.49 ± 0.009	10–20	0–10
Model 6	13 ± 1.0	2	6.8 ± 0.00	0.39 ± 0.010	20–30	0–10
Model 7	23 ± 4.3	12	6.8 ± 0.05	0.21 ± 0.040	10–20	10–20
Model 8	10 ± 0.6	1	6.8 ± 0.00	0.49 ± 0.007	20–30	350–360
Model 9	10 ± 3.6	1	6.7 ± 0.04	0.57 ± 0.034	30–40	340–350
Model 10	10 ± 0.2	1	7.1 ± 0.00	0.53 ± 0.004	0–10	10–20
Model 11	10 ± 1.4	1	7.0 ± 0.05	0.37 ± 0.031	10–20	0–10
Model 12	8 ± 1.4	3	6.9 ± 0.00	0.51 ± 0.014	20–30	340–350
Model 13	6 ± 1.3	5	7.0 ± 0.00	0.38 ± 0.012	10–20	0–10
Model 14	14 ± 2.6	3	7.0 ± 0.02	0.31 ± 0.021	0–40	0–10
Model 15	14 ± 2.2	3	7.0 ± 0.01	0.28 ± 0.014	0–40	10–20

[a]dip directions of both the slab Moho and slab top are set at 11° in all the Models 0–15, and the default back azimuthal sampling interval is 2°; [b]DD-1 and DD-2 from PCA estimation refer to two Dip Directions (DDs) derived from the two polarity shifts in the second components (Figure S6 in Supporting Information S1); [c]"±5°" refers to the intrinsic uncertainty of PCA due to RFs being stacked in 10° bins; [d]the symbol "/" indicates that the dip direction cannot be identified by this method; [e]DDS results of Models S1–S7 are listed in Table S1 in Supporting Information S1. Model descriptions are listed in Text S3 in Supporting Information S1.

3.3. Comparison With PCA Method

We benchmark DDS with PCA for synthetic Models 0–12. DDS and PCA results are listed and compared in Table 1. We find that DDS overperforms PCA in accuracy, robustness, and flexibility. First, DDS provides estimates with higher resolution and accuracy than PCA. The deviations of DDS results are mostly ≤3°, while PCA provides estimates with deviations of about 10–20° for most cases (Table 1). The lower accuracy of PCA is partly caused by the lower resolution (about 10°) due to the back azimuthal stacking. Another reason is that PCA estimates from the two polarity reversals are generally inconsistent, producing larger uncertainty in estimation (Table 1). Furthermore, DDS is more robust than PCA, especially in the case with incomplete or uneven distribution of RFs in back azimuth (Models 2–3 and 14–15). For example, in Model 2 in which RF data have a ∼180° back azimuthal gap, the deviation of PCA result is 30–40° (Figure S6b in Supporting Information S1) while the deviation of DDS result is only 1° (Figure 2a). Finally, DDS is more flexible because it can constrain dip directions from the positive and negative Ps phases separately, while PCA cannot separate the two phases and provides an average estimate. More details of PCA results and the comparison with DDS are presented in Text S4 in Supporting Information S1.

4. Application of the DDS Method in Sumatra

Our target region for DDS application is the Sumatran subduction zone, which is an extremely active tectonic zone but sparsely instrumented with broadband seismic networks. Due to the sparsity of the local networks, the resolution of available earthquake catalogs (e.g., the USGS catalog, earthquake.usgs.gov/earthquakes/search/) is at the level of global average, with an uncertainty of ∼10–20 km in both epicenter and focal depth. The spatial resolution of passive-source seismic tomography is even lower, at about 1–2° (e.g., Liu et al., 2019). Thus, both earthquake location and passive-source tomography cannot present the slab with high resolution. Several

2D marine active-source surveys have imaged the slab morphology at higher resolutions (Cook et al., 2014; Huot & Singh, 2018; Qin & Singh, 2018; Singh et al., 2008, 2012; Singh, Carton, et al., 2011). However, these active-source models are sparse. In any case, such 2D profiles cannot be used to estimate slab dip directions. Therefore, both the slab geometry and slab layering in the Sumatran subduction zone remain poorly constrained.

4.1. Tectonic Settings

In Sumatra, besides megathrusts, the oblique convergence between the Australian and Sunda plates is accommodated by a sliver plate, which slides along the trench-parallel direction. The interface between the sliver plate and the overriding Sunda plate is the Sumatran Fault Zone, located along the southern part of the Sumatra island (Liu et al., 2019; McCaffrey, 2009). The Australian plate subduction initiated at ~40 Ma when the Wharton fossil ridge ceased spreading, and integrated with the Indian plate to subduct beneath the Sunda plate, thus producing a classic double-arc tectonic feature (Jacob et al., 2014). The inner volcanic arc is parallel to the Sunda trench, while the outer ridges are highlands on the accretionary wedge above the sea level, where forearc islands, including Simeulue, Nias, Siberut, Pagai, and Enggano, compose the outer arc. The basin between the inner and the outer arcs is the Sumatran forearc basin (Figure 4).

The strike of the Sunda trench varies along the Sumatran subduction zone. Seismic tomography models show that the geometry of the subducting Indo-Australian slab is complicated, and it is associated with strong deformations such as slab bending, folding, tearing, and slab holes (Hall & Spakman, 2015; Koulakov et al., 2016; Liu et al., 2019; Pesicek et al., 2008). Singh, Hananto, Mukti, et al. (2011) use active-source seismic data and report a subducted seamount, pointing out that the mantle wedge is serpentinized by the water released from fluid-rich sediments, which then governs the aseismic slip and earthquake segmentation. Seismic tomography results indicate that the magmatic architecture and feeding system of Sumatran volcanoes are also associated with the ascending water from slab dehydration (Koulakov et al., 2016). However, questions related to structural signature of fluid-wedge interaction are still unanswered. For example: Will slab dehydration smear the interface between the subducted slab and the overriding wedge? Can we identify the causes of such smearing by resolving the dip angle or dip direction of the slab-related discontinuities? Does smearing differ between the inner and outer arcs region due to depth variation? To address these questions, we apply the new DDS method to RF data in the Sumatran subduction zone to detect the slab geometry and layering features and their variations along the strike.

4.2. Data

DDS requires clearly recognized Ps phases with back azimuthal variation as the input. The Ps phases converted from slab-related discontinuities at the subducting plate boundary are characterized as a negative-positive pulse pair. The pair of Ps phases are expected to be recognizable in the forearc areas where the oceanic crust has not (adequately) eclogitized thus preserves a strong velocity contrast against the overlying continental lithosphere (Kawakatsu et al., 2009; Kawakatsu & Watada, 2007; Kim et al., 2021; Yuan et al., 2000). We collect permanent broadband seismic data from the IA network from January 2014 to December 2016 and mobile broadband data from the ZB network from May 2008 to October 2008 (Figure S7 in Supporting Information S1). Tele-seismic events with magnitude larger than 5.5 are used to detect sensor misorientation and derive RFs with Gaussian filtering parameters of 1.5 and 2.5 (Text S5 and Figure S8 in Supporting Information S1).

After initial data quality control and visual inspection of RF waveforms, we select four permanent stations (MKBI, EGSI, GSI, and SISI from the IA network) and one mobile station (X10S from the ZB network) that are deployed in the forearc areas to study slab dip directions (Figure 4; Table S2 in Supporting Information S1). The MKBI station is located on the main island and the rest are located on the outer ridge islands (Figure 4a). In total, about 800 high-quality RFs are used for further analysis, ranging from 40° to 110° in back azimuth (Figure 4b) and distributing relatively evenly in epicenter distance (ray parameter around 0.04–0.08 s/km). The other four permanent stations in the forearc area do not show clear dipping interface-related features (Figure 4a and Figure S7 in Supporting Information S1). The negative detection could be due to the contamination by noise, and/or multiples from intra-crustal discontinuities, and/or strong heterogeneity within the slab crust.

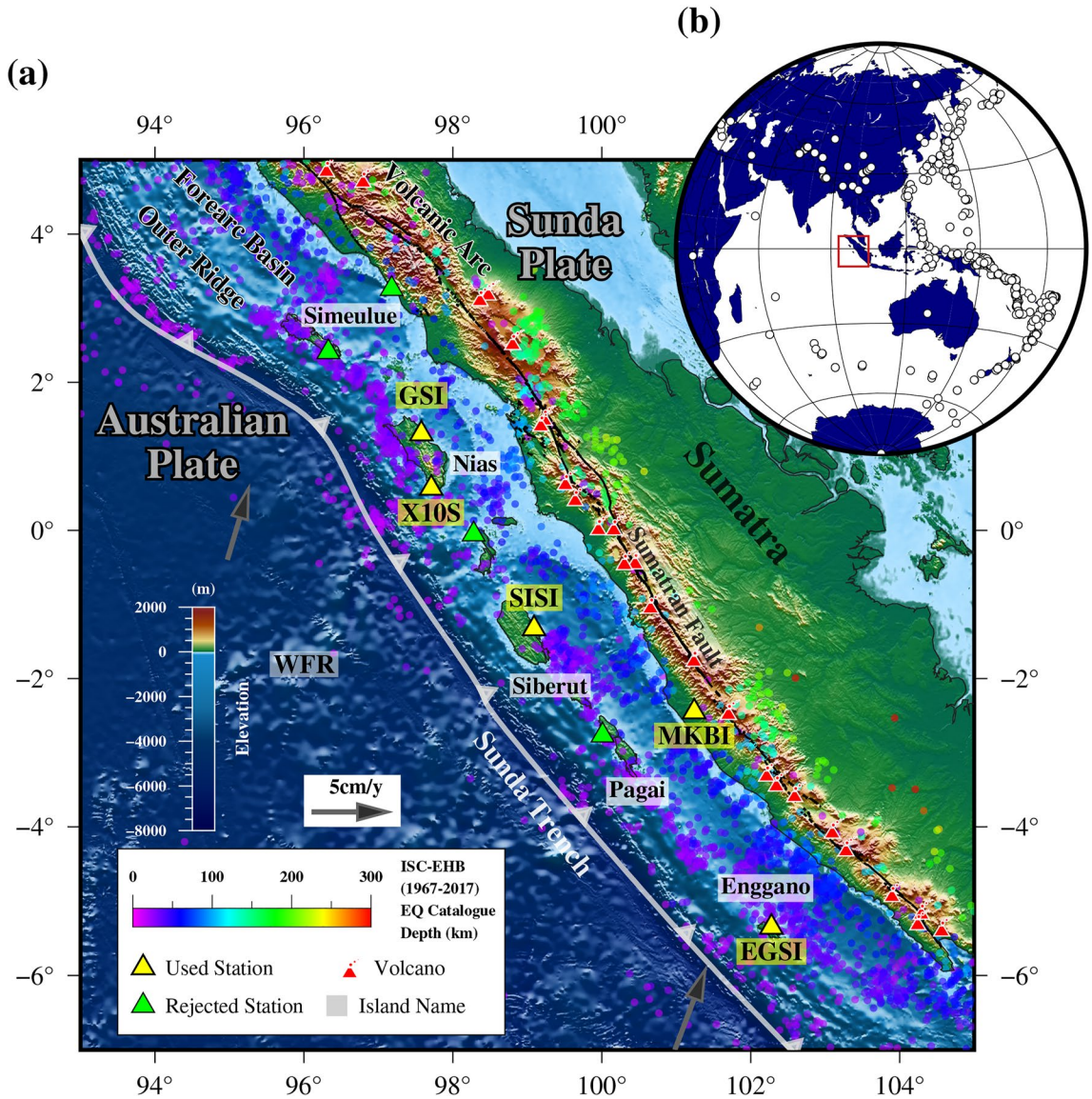

Figure 4. Location of the seismic stations and the regional geology of the Sumatran subduction zone. The yellow and green triangles denote the locations of the five stations used and four stations rejected in this study, respectively. The small colorful dots represent the epicenters of earthquakes (1964–2017) in the ISC-EHB catalog (Engdahl et al., 1998, 2020; Weston et al., 2018). The red triangles show the volcanoes active since the Holocene (Global Volcanism Program, 2013). The names of the outer ridge islands are noted in white semi-transparent labels. The "WFR" label marks the location of Wharton Fossil Ridge. The white dots at subplot (b) are the locations of the earthquakes used in our study. The plate relative velocities are modified from McCaffrey (2009).

4.3. Dip Direction Estimations

The pair of negative (arrive earlier) and positive (arrive later) phases in the selected stations arrive at around 3–10 s with clear cosine back azimuth dependence, which is also observed in T-RFs with polarities flipping (Figure S9 in Supporting Information S1). The two phases most likely reflect the presence of a dipping low-velocity layer (LVL), with the positive and negative phases being the Ps phases converted from the lower and upper boundary of the LVL, respectively. We then apply the DDS method to these phases to derive dip directions and the associated layering structure (Tables 2 and 3; Figure 5), supplemented with the estimates from PCA and TRFA (Text S6, Figures S9–S10, and Tables S3–S4 in Supporting Information S1). In DDS analysis, the average of the results from the two frequencies (~0.5 and ~0.8 Hz) is defined as the final dip direction estimate. Such an estimate is made only when the uncertainty at each frequency is <~10°.

Table 2
Dip Direction Estimates for Sumatran Stations (Gaussian Coefficient of 2.5)

	DDS for the positive phase			DDS for the negative phase		
Station	DD (°)	CT (s)	Amp (s)	DD (°)	CT (s)	Amp (s)
X10S	90 ± 35.1	4.0 ± 0.29	0.40 ± 0.195	64 ± 6.6	2.7 ± 0.08	0.54 ± 0.087
EGSI	48 ± 3.9	4.2 ± 0.07	0.70 ± 0.121	49 ± 3.4	2.8 ± 0.08	0.70 ± 0.096
GSI	251 ± 27.8	4.6 ± 0.20	0.93 ± 0.218	[a]	[a]	[a]
SISI	55 ± 3.6	5.2 ± 0.09	0.96 ± 0.121	34 ± 6.3	3.8 ± 0.18	0.38 ± 0.249
MKBI	47 ± 2.5	8.7 ± 0.05	0.79 ± 0.053	70 ± 10.1	6.7 ± 0.20	0.81 ± 0.206

Note. DD means dip direction, CT means central time, and Amp denotes amplitude.
[a]Denotes no estimation for the negative phase due to its absence in RF waveforms.

The negative and positive phases arrive at about 3.1 and 4.5 s on the four outer ridge stations and at about 6.7 and 8.7 s on the main island station MKBI (Figures 4 and 5). For the MKBI station, at ∼0.5 Hz, DDS shows that the dip directions for the negative and positive phases are 47 ± 2.5° and 70 ± 10.1°, respectively, similar to those estimated at ∼0.8 Hz (44 ± 2.6° and 66 ± 6.3°), as well as those from the TRFA on the Ps phases (40–50° and 50–60°), and that from the PCA (40–60°). The final DDS estimates for the negative and positive phases are 45.5 ± 2.55° and 68 ± 8.2°, respectively, indicating a ∼23° dip direction difference between the upper and lower interfaces of the LVL. Similar to station MKBI, the azimuthal profiles of the two phases for EGSI and SISI stations also fit well with cosine functions (Figure 5). The dip direction estimation for EGSI is 47 ± 5.3° for the positive phase, close to that estimated from the negative phase (49.5 ± 2.8°). The discrepancy is merely 2.5° and less than the uncertainties. The dip direction of SISI derived from the positive phase is 52.5 ± 3.6°, which is much larger, with a difference of 14°, than that obtained from the negative phase (38.5 ± 5.2°). The uncertainty of the dip direction estimation for X10S from the positive phase is larger than 30°, mostly due to the insufficient data (only 69 RFs; Table S2 in Supporting Information S1), so we discard the estimation from further interpretation. DDS produces two dip direction candidates for GSI: 251° and 70° (Figure 5g). Although 251° is more consistent with the PCA estimation (230–300°), we prefer the dip direction of 70°, because of its smaller uncertainty, and better consistency with the Slab2 model and the result from the neighboring station (X10S). The two dip direction candidates are likely due to the interference between the noise/crustal multiples and the targeted Ps phases, which produces artifacts in both DDS and PCA results. At 0.8 Hz, DDS does not identify the negative phase, so we determine the dip directions beneath GSI only at 0.5 Hz. The final dip direction is 70 ± 10.7° for the positive phase and 72 ± 9.9° for the negative phase.

In general, the dip directions estimated by DDS are consistent with results from PCA and TRFA, but with higher resolution (Figure 6). We also mark the relative reliability between DDS estimates by three quality levels (A, B, and C), with "A" marking well-fitted results, "B" marking non-unique estimations, and "C" denoting those with uncertainty >30° (Figure 6). To further justify the robustness of DDS estimate, we conduct DDS for RFs after stacking in back azimuthal bins. This procedure is named as post-Stacking Dip Direction Searching strategy (SDDS) (Text S7, Figures S11–S12, and Table S4 in Supporting Information S1). SDDS estimates are broadly consistent with those of DDS but with larger uncertainties (a few to dozens of degrees) than the DDS results (Figure 6).

Table 3
Dip Direction Estimates for Sumatran Stations (Gaussian Coefficient of 1.5)

	DDS for the positive phase			DDS for the negative phase		
Station	DD (°)	CT (s)	Amp (s)	DD (°)	CT (s)	Amp (s)
X10S	81 ± 36.6	4.0 ± 0.22	0.34 ± 0.222	65 ± 6.1	2.6 ± 0.06	0.55 ± 0.063
EGSI	46 ± 6.6	4.2 ± 0.07	0.65 ± 0.121	50 ± 2.2	2.8 ± 0.03	0.76 ± 0.045
GSI	70 ± 10.7	4.7 ± 0.24	1.34 ± 0.278	72 ± 9.9	3.4 ± 0.13	1.48 ± 0.227
SISI	50 ± 3.5	5.1 ± 0.07	0.89 ± 0.115	43 ± 4.1	3.4 ± 0.12	0.86 ± 0.152
MKBI	44 ± 2.6	8.7 ± 0.04	0.96 ± 0.050	66 ± 6.3	6.7 ± 0.08	0.73 ± 0.075

Note. DD means dip direction, CT means central time, and Amp denotes amplitude.

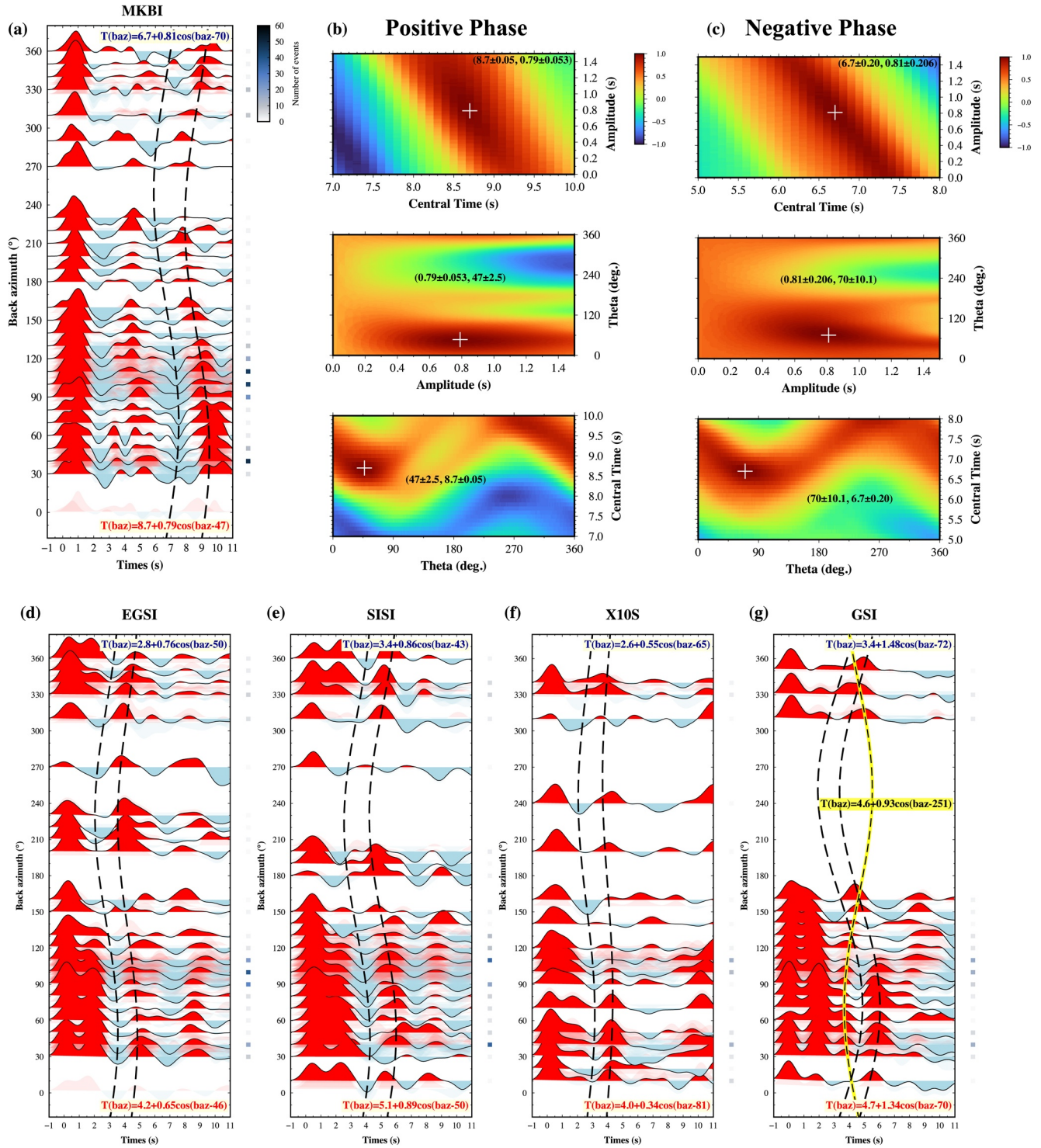

Figure 5. Dip Direction Searching (DDS) for real data. Figures (a)–(c) show DDS results for station MKBI. Figure (a) shows receiver functions (RFs) constructed at ~0.8 Hz. Stacked RFs in 10° back azimuthal bins are shown in bright red and blue, and RFs before stacking are colored semi-transparently. Small squares and the colorbar on the right side indicate the number of RFs stacked in each bin. Figure (b) is the DDS searching plot for the positive phase, and (c) is the plot for the negative phase. The optimal cosine functions for the positive and negative phases are labeled in the same colors as in (a). Figures (d)–(g) are the same as in (a) but for stations EGSI, SISI, X10S, and GSI, respectively, and for RFs constructed at ~0.5 Hz. The yellow label and yellow line in (g) indicate another possible candidate of DDS estimation.

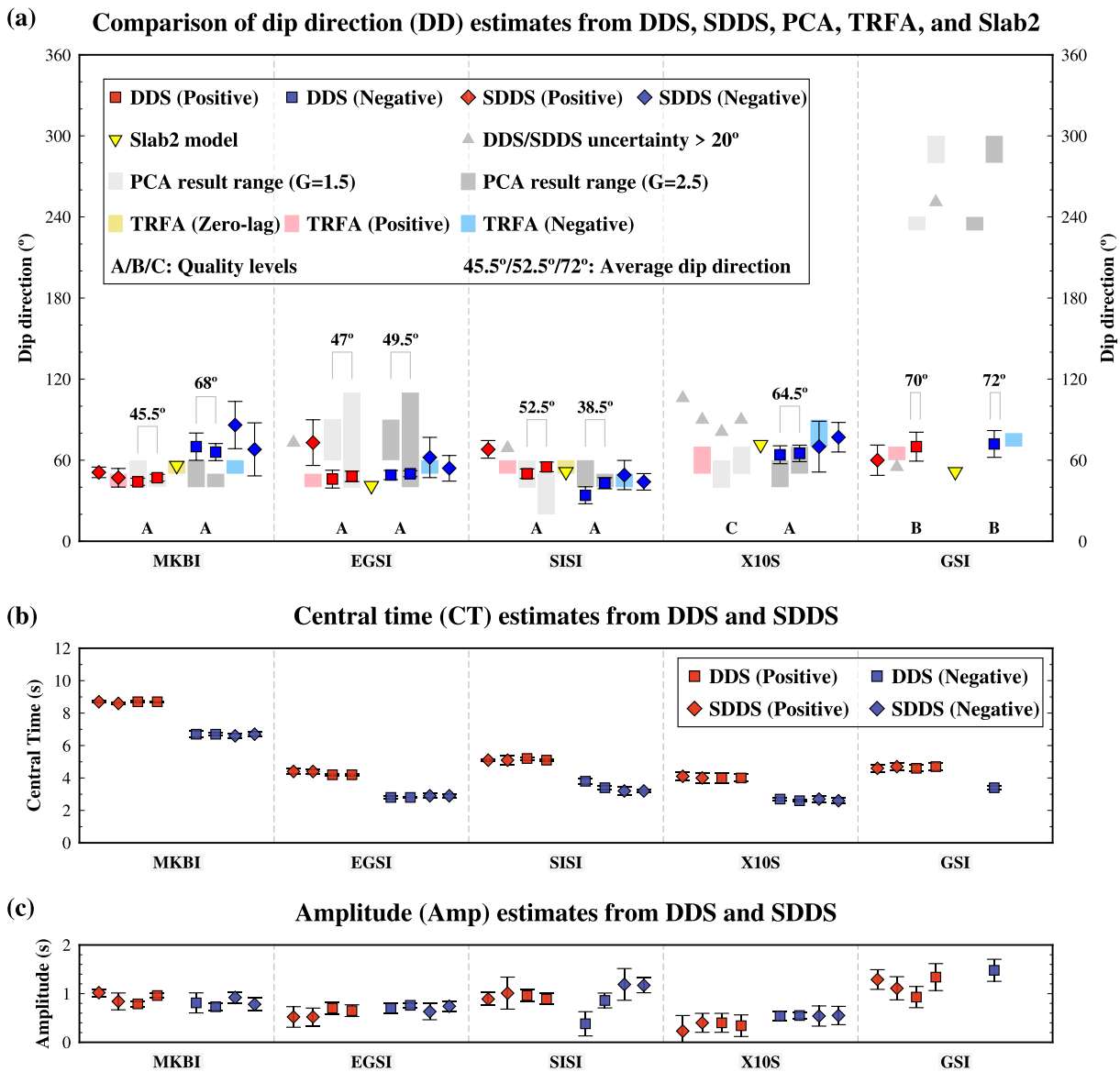

Figure 6. Dip direction results derived from Dip Direction Searching (DDS), principal component analysis (PCA), and Transverse Receiver Function Analysis (TRFA). (a) The red and blue colors indicate results for positive and negative phases, respectively, with DDS estimates as squares and post-stacking DDS (SDDS) estimates as diamonds. Both the results are obtained at 0.8 and 0.5 Hz. The gray triangles show DDS and SDDS estimates with uncertainties >20°, which are not considered in the discussion. The inverse yellow triangles show dip directions extracted from the Slab2 model beneath the stations. TRFA estimates from the zero-lag phase, the positive phases, and the negative phases are shown by the light yellow, light red, and light blue bars, respectively. (b) and (c) indicate DDS and SDDS central time and amplitude results, respectively.

Another possibility accounting for the cosine variation is an anisotropic layer with plunging symmetric axes (Levin & Park, 1997; J. Li et al., 2019; P. Wang et al., 2010). However, this scenario is less possible or it plays a secondary role when considering the tectonic setting and other independent evidence. In particular, the dip directions (Figures 6 and 7) and the depth of the dipping layer we obtained are highly consistent with the Slab2 model (Section 4.4), strongly suggesting that the pair of Ps phases is caused by a dipping LVL associated with slab interfaces.

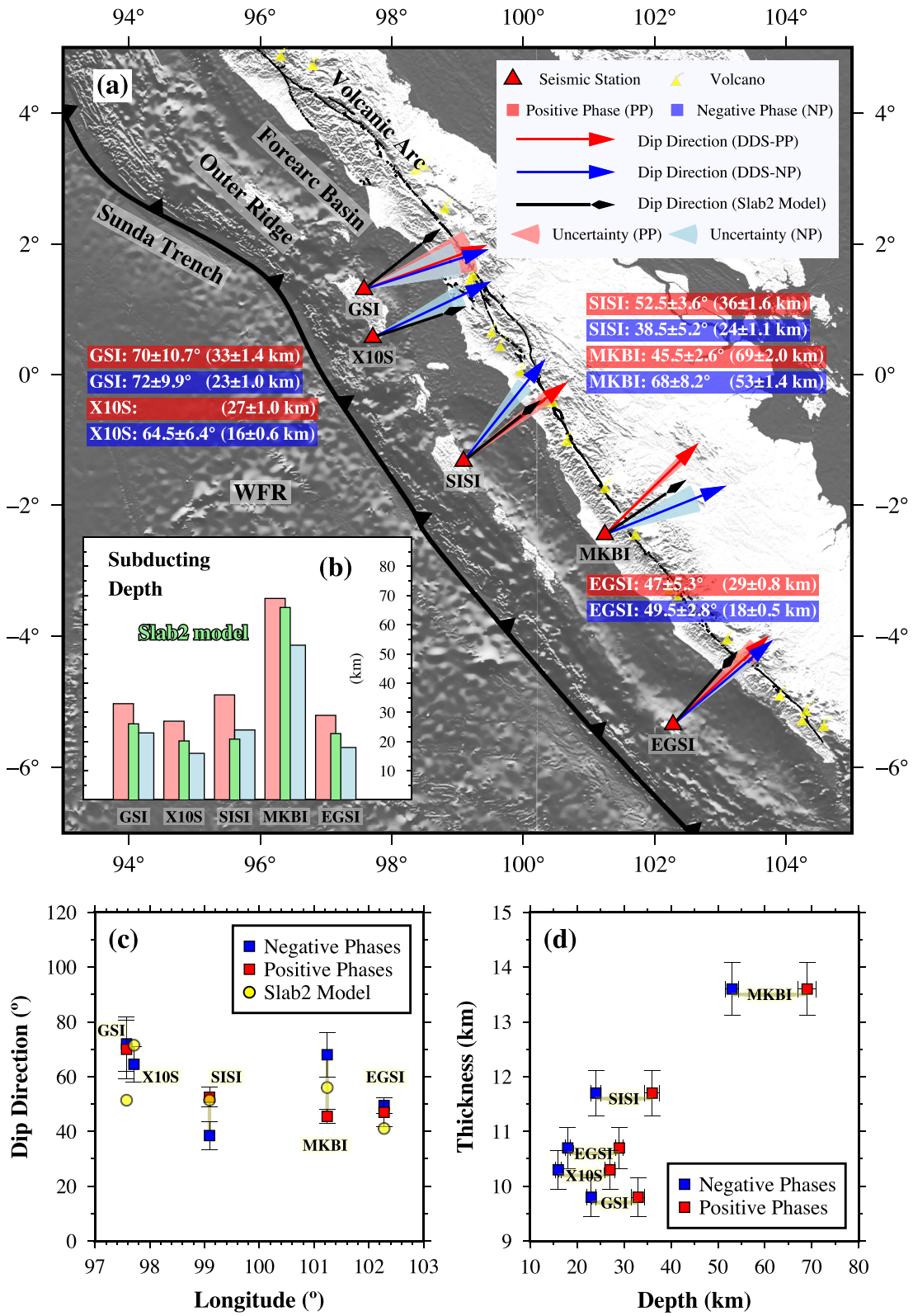

Figure 7. Spatial variation of dip directions estimated by Dip Direction Searching (DDS). Figure (a) shows the dip direction estimates. The red and yellow triangles denote the location of the five stations and the arc volcanoes, respectively. Other descriptions are the same as in Figure 4. Figure (b) shows the subducting depth estimation. The red, blue, and green bars represent the subducting depths of the lower boundary of the low-velocity layer (LVL), the upper boundaries of the LVL, and the slab surface from the Slab2 model, respectively. Figure (c) shows the relationship between dip direction and longitude. Figure (d) shows the positive correlation between subducting depth and thickness of the LVL.

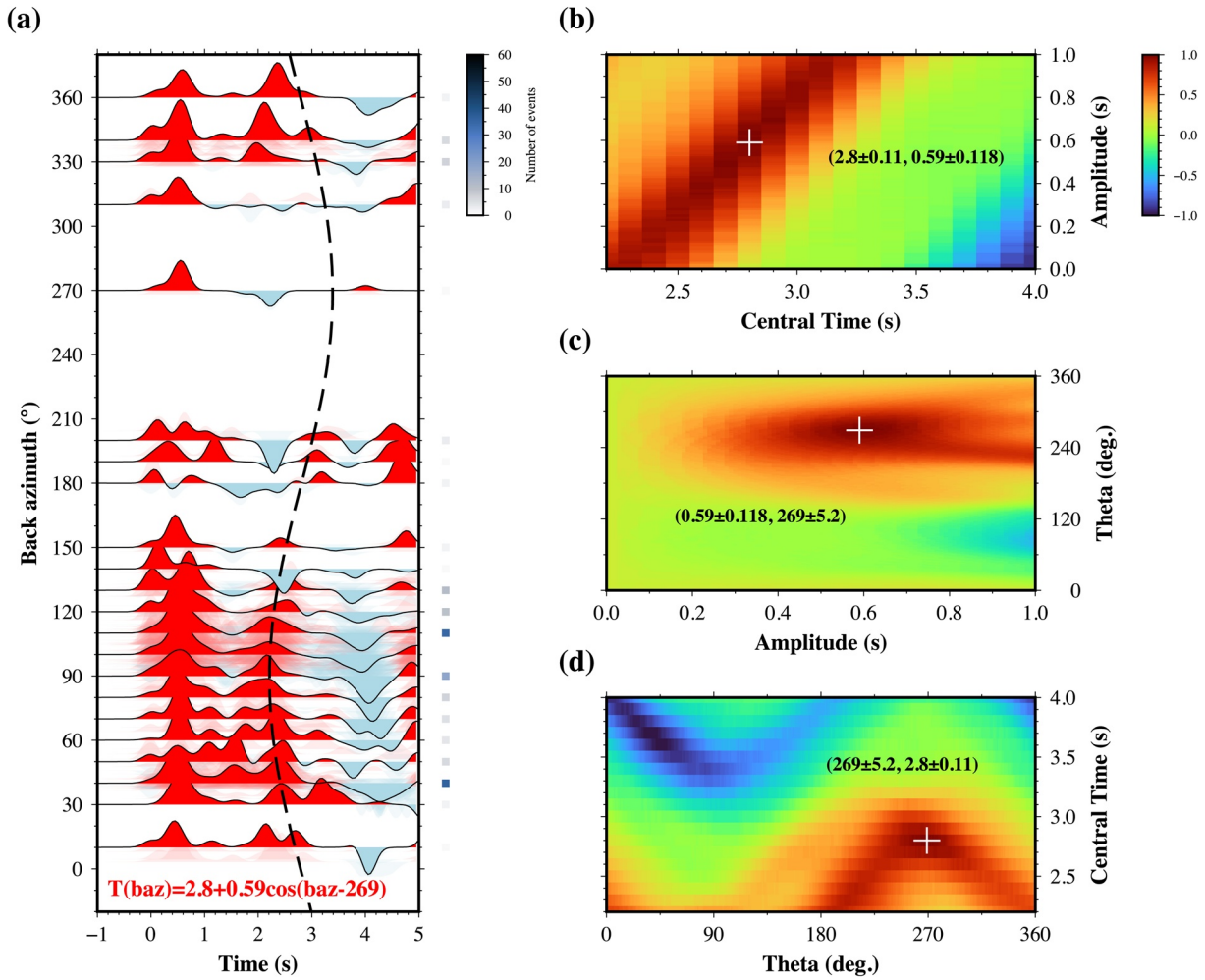

Figure 8. Dip Direction Searching for shallow dipping structures at station SISI. The receiver functions are calculated with a Gaussian coefficient of 5.0 (~1.6 Hz). Other descriptions are the same as in Figure 5.

4.4. Depth of Dipping Velocity Interfaces

The depth of the upper boundary of the LVL is estimated by converting the central time of the negative phases to depth based on a local 1D velocity model (Collings et al., 2012) using the ray-tracing formula assuming horizontal layers. This assumption is reasonable for rays coming along the strike directions. The central times of the negative phases range from ~2.7 to 6.7 s, corresponding to the depths of 16–53 km, which is 3–13 km shallower (except SISI which is deeper) than the Slab2 model (Figure 7b). The thickness of the LVL is estimated based on the central time difference between the positive and negative phases. According to previous studies (e.g., Guo et al., 2021; Kawakatsu & Watada, 2007; Yuan et al., 2000), we assume the LVL as an oceanic crust. Seven different oceanic crustal velocity models—from lithological measurements (gabbro, greenschist, and amphibolite facies metagabbro) (Christensen, 1978), from Crust1.0 (Laske et al., 2012) in the Indian Ocean, from the Cascadia subduction zone (Tauzin et al., 2017) and from the Japan subduction zone (Wirth & Long, 2012)—are considered for the LVL thickness calculation (Text S8 in Supporting Information S1). The resulting thicknesses range from ~10 to ~14 km with uncertainties of 0.3–0.5 km (Figure S13a in Supporting Information S1). The depth of the lower boundary of the LVL is estimated by adding the vertical thickness to the depth of the LVL upper boundary. The resulting depth estimates are 27–69 km, which are 3–15 km deeper than the Slab2 model (Figure 7b). Uncertainties of the depth and thickness estimates are ≤2 km, defined and analyzed in Text S8 in Supporting Information S1.

4.5. DDS for Shallow Structures

A positive signal at ~2 s with a clear cosine dependence in back azimuth is observed at stations SISI and GSI, indicating a dipping structure at shallower depths (Figure 8 and Figure S14 in Supporting Information S1). We apply DDS to the data at the higher frequencies of ~1.6 and ~2.5 Hz (Gaussian coefficients of 5.0 and 8.0, respectively). At 1.6 Hz, the dip direction and central time at SISI are 269 ± 5.2° and 2.8 ± 0.11 s, respectively (Figure 8), consistent with the results of 262 ± 8.5° and 2.9 ± 0.14 s derived at 2.5 Hz. The uncertainty is calculated by a bootstrapping method but keeping only those dip direction estimates that fall within 45° of the DDS estimate (Figure S15 in Supporting Information S1). Using the local velocity model, we estimated the depth of the dipping discontinuity to be 18 ± 1.1 km. At GSI station, consistent dip directions (45 ± 10.7° and 52 ± 9.1°) and central times (1.7 ± 0.18 s and 1.6 ± 0.14 s) are also estimated at the two frequencies, respectively (Figure S14 in Supporting Information S1). The depth is estimated to be 8 ± 1.0 km. These results demonstrate that DDS can identify not only dip directions of slab discontinuities, but also any other dipping discontinuities as shallow as above 10 km depth.

5. Discussion on Sumatra Subduction

5.1. Nature of the LVL

The LVL, associated with the subducting oceanic crust, has been detected in many subduction zones by RF studies (Ai et al., 2005; Audet et al., 2009; Audet & Kim, 2016; Bostock, 2013; Ferris et al., 2003; Hansen et al., 2012; Kawakatsu & Watada, 2007; X. Li et al., 2000; Tauzin et al., 2017; Ward et al., 2018; Yuan et al., 2000). However, the interpretation of the LVL is hotly debated (Bostock, 2013). The LVL is generally interpreted as the subducting oceanic crust at depths shallower than 80 km when the thickness of LVL is around the average oceanic crust thickness (Ai et al., 2005; Chen et al., 2005; Kawakatsu & Watada, 2007; Kim et al., 2021; X. Li et al., 2000; Tauzin et al., 2017; Ward et al., 2018; Yuan et al., 2000). Other studies interpret the LVL as (a) the upper oceanic crust when the LVL is thin as ~3–4 km and with an extremely high Vp/Vs ratio (>2.45) (e.g., Audet et al., 2009; Bostock, 2013; Hansen et al., 2012), (b) a combination of the oceanic crust and a serpentinized mantle layer if the thickness is estimated to be >10 km (e.g., Ferris et al., 2003), (c) or a fluid-filled shear zone if the LVL is observed above the oceanic crust (Audet & Schaeffer, 2018; Calvert et al., 2020; Nedimović et al., 2003).

Here, we find the LVL is located around the slab surface (Figure 7b) and thus associates the LVL with the oceanic crust. The dip direction difference between the upper and lower boundaries of the LVL is less than 3° beneath GSI and EGSI stations, suggesting that the two boundaries are parallel beneath Nias and Enggano islands. The differences are as high as 14° and 22.5° for SISI and MKBI stations, respectively, which implies the two boundaries are non-parallel beneath the Siberut and Pagai island areas (Figures 7a and 7c). Using normal oceanic crustal velocity models, the estimated thickness of the LVL is 10–14 km (±0.3–0.5 km) (Figure S13a in Supporting Information S1), much larger than the global average of the oceanic crust thickness (~6–7 km) and that in the Indian Ocean (~3.5–7 km) (Laske et al., 2012; Qin & Singh, 2015; Singh, Carton, et al., 2011).

We interpret that the abnormally thick LVL with dip direction discrepancy as a partial serpentinization layer above the hydrated oceanic crust or subducting seamounts/oceanic plateaus (Ferris et al., 2003; Singh, Hananto, Mukti, et al., 2011). Both the subducting seamounts and the serpentinized mantle wedge have been observed in the Sumatran subduction zone (Singh, Hananto, & Chauhan, 2011; Singh, Hananto, Mukti, et al., 2011). We prefer the partial serpentinization model because the thick LVL is observed at all five stations; that is, it is less likely that all these stations sampled seamounts or oceanic plateaus. Serpentinization decreases the velocity contrast between the gabbro-dominated oceanic crust and the peridotite-dominated mantle, smearing the plate boundary and making the slab top more difficult to be detected (Bostock et al., 2002; Carlson & Miller, 2003; Christensen, 2004; Ferris et al., 2003). In this scenario, the upper boundary of the LVL indicates the serpentinization front in the mantle wedge, and the lower boundary indicates the oceanic Moho. The serpentinization front undulates along both strike and dip directions, and thus produces a dip direction difference between the two boundaries. This mechanism can also explain the generally shallower top boundary of the LVL than the Slab2 model (Figure 7b) and the positive correlation between the thickness and depth of the LVL (Figure 7d). The positive correlation is also reported in the Cascadia subduction zone (Audet & Schaeffer, 2018). We consider the positive correlation observed in Sumatra as a result of serpentinization induced by slab dehydration, which is enhanced with the increase of depth, pressure, temperature, and metamorphism (e.g., eclogitization) as the oceanic crust descends (Figure 9) (Carlson & Miller, 2003; Christensen, 2004).

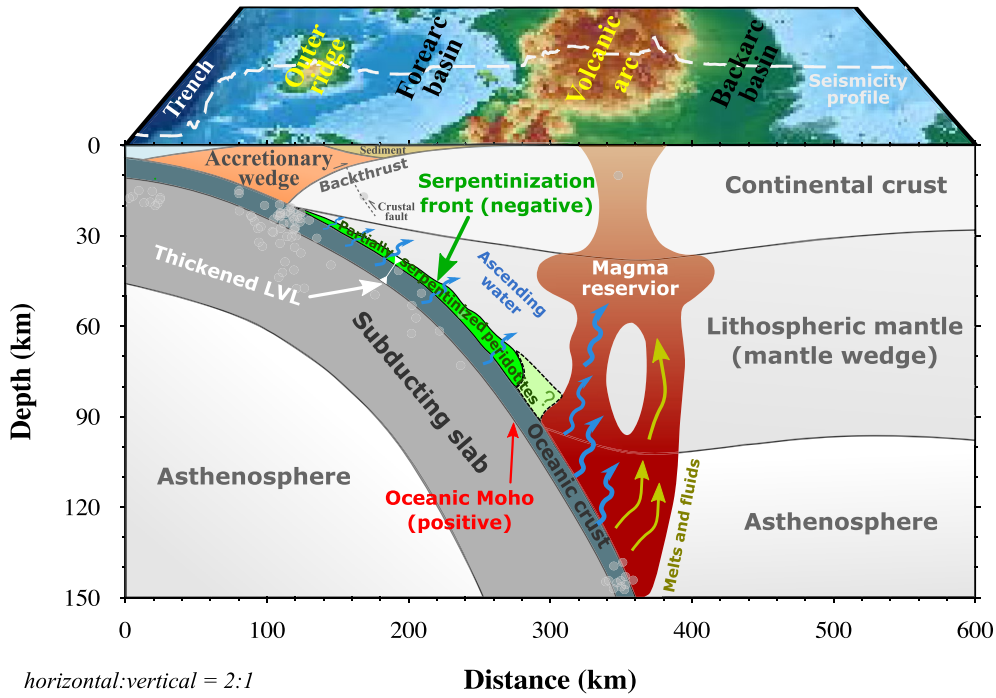

Figure 9. A conceptual model of a partially serpentinized peridotite layer above the oceanic crust. The semi-transparent gray dots represent the earthquakes in Figure 4 within 20 km from the seismicity profile. The profile is marked as the dashed white line. The accretionary wedge dipping structures are modified from X. Wang et al. (2018) and Singh, Hananto, and Chauhan (2011). The dashed gray line shows the reactivated fault within the forearc crust (X. Wang et al., 2018). The magmatic architecture is taken from Koulakov et al. (2016). The question mark indicates the unknown compositional transition from partially serpentinized peridotites to ascending melts and fluids that feed the volcanic arc.

We note that there is a trade-off between the LVL thickness and the Vp/Vs estimations (Figure S13b in Supporting Information S1). If we assume a constant LVL thickness of 7 km, which is a global average of oceanic crust thickness, the estimated Vp/Vs ranges 2.2–2.7 (Figure S13b in Supporting Information S1). Such high Vp/Vs requires a pore-fluid abundant oceanic crust with a sealed plate boundary (Audet et al., 2009; Hansen et al., 2012). However, this also requires a highly varying volume of pore-fluid to produce a wide range of Vp/Vs, and an increase of the pore-fluid volume with depth (i.e., a Vp/Vs >~2.5 at ~70 km depth beneath station MKBI). The latter also requires that the plate boundary remains sealed down to a depth of 70 km. These conditions are considered more difficult to be met compared with the partial serpentinization model. While we acknowledge that more studies are required to scrutinize the pure oceanic crust model, the partial serpentinization model is preferred for the Sumatran subduction zone.

5.2. Slab Internal Deformation

We define the dip direction of the slab Moho (i.e., the lower boundary of the LVL) as the dip direction of the slab, because the Moho experiences less deformation and metamorphism than the upper boundary of the LVL (e.g., Kawakatsu & Watada, 2007). The dip direction of the slab Moho is 70 ± 10.7° below the Nias island at the depth of 33 ± 1.4 km in the northwest, gradually decreasing to 47 ± 5.3° beneath Enggano Island at the depth of 29 ± 0.8 km in the southeast. At the depth of 69 ± 2.0 km, the dip direction changes to 45.5 ± 2.6° below the mainland margin near Pagai Island (Figure 7). These dip direction estimates agree well with the Slab2 model (Figures 6 and 7). The continuous variation of slab dip direction along the Sunda trench (Figure 7c) implies slab folding or tearing, also noted in travel time tomography studies (Liu et al., 2019, 2021). The slab folding may be a result of the oblique subduction of the Australian plate (Liu et al., 2019; McCaffrey, 2009), or the lateral bending of the Australian plate, which is increasingly driven by gravity on the east side of the Wharton fossil ridge as the plate cools down.

6. Limitations of DDS and Future Work

While DDS is a robust method for quantifying dip directions of slab discontinuities at a high precision, three limitations need to be taken into consideration. First, DDS is based on the hypothesis that anisotropy strength of the media above the dipping discontinuity is weak (<5–10% in the mantle wedge and <2%–5% in the crust). Larger anisotropy (e.g., 10% mantle wedge anisotropy and 5% crustal anisotropy) with the symmetric axis oriented toward certain azimuths could impose ∼10° deviation in DDS estimation (Model 7; Figure S3 in Supporting Information S1). Second, DDS is applicable when the dip angle of the LVL is less than ∼35°. For a larger dip angle (e.g., 45°), the Ps phases converted from the LVL will present polarity changes (Figure 3e), because some of the rays coming from updip azimuths actually sample the downdip end of the dipping interfaces. If RFs mostly sample the azimuths with polarity changes, DDS will provide a poor estimation (Figure 3g). Third, the targeted phases should be free from the interference with other nearby signals (e.g., the direct P-wave, multiples associated with shallower discontinuities, or scattering from small-scale heterogeneities), which may partly explain why DDS is not applicable to about half of the IA stations in the forearc Sumatra (Figure S7 in Supporting Information S1). Regarding interfered phases (e.g., shown for station GSI), DDS estimation would be improved with waveform modeling, which is a potential future direction of method development. As shown in Figure S4 in Supporting Information S1 and Figure 3g, polarity changes, decreases in amplitude, and presence of strong anisotropy will significantly affect the two-lobed waveform variation in back azimuth, which can be noticed by visual inspection. Visual inspection or AI-based sophisticated analysis on RF waveforms (e.g., Gong et al., 2022) is thus recommended as a necessary procedure for data quality-control.

To partially overcome these limitations, we propose to further integrate amplitude and arrival time variations of the converted phases to constrain more detailed velocity structures. The harmonic decomposition on the amplitudes of RFs (e.g., Audet, 2015; Bianchi et al., 2010) and the moveout corrections to the travel time of converted phases (e.g., Liu & Niu, 2012) are proved effective in constraining detailed anisotropic structure. Expanding these methods in revealing the geometry of dipping interfaces are suggested for future works. We also suggest that the main sources of difficulty in identifying slab phases are complex RF waveforms originating from 2D and 3D velocity structures, or from low-velocity sedimentary basins. Although basin effects on RFs could be partially suppressed (e.g., Yu et al., 2015), 2D and 3D wavefield calculations have rarely been conducted to understand the complexity in the RF waveforms. We believe this could also be an avenue to advance RF studies.

7. Conclusion

We have developed a DDS method to constrain dip directions and layered structures of slab-related discontinuities, and verify the precision and robustness of the method with a series of synthetic tests. As a case study, we apply DDS to the Sumatran subduction zone to constrain the geometry and nature of the subduction plate boundary. We detect a dipping LVL with unparallel upper and lower boundaries beneath central Sumatra. The LVL is much thicker than the oceanic crust and its thickness increases with depth. We interpret the thick LVL as consisting of both the subducting oceanic crust and a partial serpentinization layer attached at the top, forming a diffuse plate boundary. Our case study demonstrates that DDS can constrain slab geometry and structure with sparse seismic data, and thus might be applicable to other subduction zones and for various dipping interfaces.

Data Availability Statement

Synthetic waveforms were produced by RAYSUM (Frederiksen & Bostock, 2000). Seismic data used in this study have been archived at the WDC for Geophysics, Beijing (http://wdc.geophys.ac.cn/ArticleDataInfo.asp?MetaId=408 or https://doi.org/10.12197/2022GA009). The seismic data of IA network are achieved at the GEOFON center with restricted access currently. The authors downloaded the IA network data from 202.90.198.100/webdc3/ when it was accessible. The seismic data of ZB network were accessed from IRIS (www.iris.edu; open access). DDS and PCA codes are available from Mingye Feng (fmy@mail.iggcas.ac.cn or fengmycn@gmail.com) upon request. All links were accessed on 13 April 2022.

Acknowledgments
The authors thank Editor Michael Bostock, the Associate Editor, reviewers Dr. Pascal Audet, Dr. Vadim Levin, and another anonymous reviewer, who help to improve the quality of this paper. This research is jointly supported by the National Natural Science Foundation of China (Grant 42288201), the Strategic Priority Research Program (A) of Chinese Academy of Sciences (Grant XDA20070302) and Singapore MOE tier-2 Grant (MOE2019-T2-1-182 (S)). This research was supported by the Earth Observatory of Singapore via its funding from the National Research Foundation Singapore and the Singapore Ministry of Education under the Research Centres of Excellence initiative. This work comprises EOS contribution number 522. M. Feng thanks the Chinese Scholarship Council for scholarship fund. The authors express great appreciation to the Indonesian Agency for Meteorology, Climatology, and Geophysics for providing the seismic data. Figures were made with GMT (Wessel & Smith, 1998). L. Chen thanks the members of COFFICE 422 in IGGCAS for their helpful discussions.

References

Ai, Y., Zhao, D., Gao, X., & Xu, W. (2005). The crust and upper mantle discontinuity structure beneath Alaska inferred from receiver functions. *Physics of the Earth and Planetary Interiors*, *150*(4), 339–350. https://doi.org/10.1016/j.pepi.2004.12.002

Ammon, C. J. (1991). The isolation of receiver effects from teleseismic P waveforms. *Bulletin of the Seismological Society of America*, *81*(6), 2504–2510. https://doi.org/10.1785/bssa0810062504

Audet, P. (2015). Layered crustal anisotropy around the San Andreas fault near Parkfield, California. *Journal of Geophysical Research: Solid Earth*, *120*(5), 3527–3543. https://doi.org/10.1002/2014jb011821

Audet, P., Bostock, M. G., Boyarko, D. C., Brudzinski, M. R., & Allen, R. M. (2010). Slab morphology in the Cascadia fore arc and its relation to episodic tremor and slip. *Journal of Geophysical Research: Solid Earth*, *115*(B4), B00A16. https://doi.org/10.1029/2008jb006053

Audet, P., Bostock, M. G., Christensen, N. I., & Peacock, S. M. (2009). Seismic evidence for overpressured subducted oceanic crust and megathrust fault sealing. *Nature*, *457*(7225), 76–78. https://doi.org/10.1038/nature07650

Audet, P., & Kim, Y. (2016). Teleseismic constraints on the geological environment of deep episodic slow earthquakes in subduction zone forearcs: A review. *Tectonophysics*, *670*, 1–15. https://doi.org/10.1016/j.tecto.2016.01.005

Audet, P., & Schaeffer, A. J. (2018). Fluid pressure and shear zone development over the locked to slow slip region in Cascadia. *Science Advances*, *4*(3), 1–7. https://doi.org/10.1126/sciadv.aar2982

Bianchi, I., Park, J., Piana Agostinetti, N., & Levin, V. (2010). Mapping seismic anisotropy using harmonic decomposition of receiver functions: An application to Northern Apennines, Italy. *Journal of Geophysical Research: Solid Earth*, *115*(B12), B12317. https://doi.org/10.1029/2009jb007061

Bostock, M. G. (2013). The Moho in subduction zones. *Tectonophysics*, *609*, 547–557. https://doi.org/10.1016/j.tecto.2012.07.007

Bostock, M. G., Hyndman, R. D., Rondenay, S., & Peacock, S. M. (2002). An inverted continental Moho and serpentinization of the forearc mantle. *Nature*, *417*(6888), 536–538. https://doi.org/10.1038/417536a

Calvert, A. J., Bostock, M. G., Savard, G., & Unsworth, M. J. (2020). Cascadia low frequency earthquakes at the base of an overpressured subduction shear zone. *Nature Communications*, *11*(1), 1–10. https://doi.org/10.1038/s41467-020-17609-3

Carlson, R. L., & Miller, D. J. (2003). Mantle wedge water contents estimated from seismic velocities in partially serpentinized peridotites. *Geophysical Research Letters*, *30*(5), 1250. https://doi.org/10.1029/2002gl016600

Cassidy, J. F. (1992). Numerical experiments in broadband receiver function analysis. *Bulletin of the Seismological Society of America*, *82*(3), 1453–1474. https://doi.org/10.1785/bssa0820031453

Chen, L., Wen, L., & Zheng, T. (2005). A wave equation migration method for receiver function imaging: 2. Application to the Japan subduction zone. *Journal of Geophysical Research*, *110*(11), 1–15. https://doi.org/10.1029/2005JB003666

Cheng, C., Bodin, T., Tauzin, B., & Allen, R. M. (2017). Cascadia subduction slab heterogeneity revealed by three-dimensional receiver function Kirchhoff migration. *Geophysical Research Letters*, *44*(2), 694–701. https://doi.org/10.1002/2016GL072142

Christensen, N. I. (1978). Ophiolites, seismic velocities and oceanic crustal structure. *Tectonophysics*, *47*(1–2), 131–157. https://doi.org/10.1016/0040-1951(78)90155-5

Christensen, N. I. (2004). Serpentinites, peridotites, and seismology. *International Geology Review*, *46*(9), 795–816. https://doi.org/10.2747/0020-6814.46.9.795

Collings, R., Lange, D., Rietbrock, A., Tilmann, F., Natawidjaja, D., Suwargadi, B., et al. (2012). Structure and seismogenic properties of the Mentawai segment of the Sumatra subduction zone revealed by local earthquake traveltime tomography. *Journal of Geophysical Research: Solid Earth*, *117*(B1). B01312. https://doi.org/10.1029/2011JB008469

Cook, B. J., Henstock, T. J., McNeill, L. C., & Bull, J. M. (2014). Controls on spatial and temporal evolution of prism faulting and relationships to plate boundary slip offshore north-central Sumatra. *Journal of Geophysical Research: Solid Earth*, *119*(7), 3678–3699. https://doi.org/10.1002/2013JB010834

Efron, B., & Tibshirani, R. (1986). Bootstrap methods for standard errors, confidence intervals, and other measures of statistical accuracy. *Statistical Science*, *1*(1), 54–75. https://doi.org/10.1214/ss/1177013815

Engdahl, E. R., Di Giacomo, D., Sakarya, B., Gkarlaouni, C. G., Harris, J., & Storchak, D. A. (2020). ISC-EHB 1964–2016, an improved data set for studies of earth structure and global seismicity. *Earth and Space Science*, *7*(1), 1–13. https://doi.org/10.1029/2019EA000897

Engdahl, E. R., van der Hilst, R., & Buland, R. (1998). Global teleseismic earthquake relocation with improved travel times and procedures for depth determination. *Bulletin of the Seismological Society of America*, *88*(3), 722–743. https://doi.org/10.1785/bssa0880030722

Ferris, A., Abers, G. A., Christensen, D. H., & Veenstra, E. (2003). High resolution image of the subducted Pacific (?) plate beneath central Alaska, 50-150 km depth. *Earth and Planetary Science Letters*, *214*(3–4), 575–588. https://doi.org/10.1016/S0012-821X(03)00403-5

Frederiksen, A. W., & Bostock, M. G. (2000). Modelling teleseismic waves in dipping anisotropic structures. *Geophysical Journal International*, *141*(2), 401–412. https://doi.org/10.1046/j.1365-246x.2000.00090.x

Global Volcanism Program. (2013). Volcanoes of the World [Dataset]. Smithsonian Institution. https://doi.org/10.5479/si.GVP.VOTW4-2013

Gong, C., Chen, L., Xiao, Z., & Wang, X. (2022). Deep learning for quality control of receiver functions. *Frontiers of Earth Science*, *10*, 921830. https://doi.org/10.3389/feart.2022.921830

Gosselin, J. M., Audet, P., Estève, C., McLellan, M., Mosher, S. G., & Schaeffer, A. J. (2020). Seismic evidence for megathrust fault-valve behavior during episodic tremor and slip. *Science Advances*, *6*(4), eaay5174. https://doi.org/10.1126/sciadv.aay5174

Guo, H., McGuire, J. J., & Zhang, H. (2021). Correlation of porosity variations and rheological transitions on the southern Cascadia megathrust. *Nature Geoscience*, *14*(5), 341–348. https://doi.org/10.1038/s41561-021-00740-1

Hall, R., & Spakman, W. (2015). Mantle structure and tectonic history of SE Asia. *Tectonophysics*, *658*, 14–45. https://doi.org/10.1016/j.tecto.2015.07.003

Hansen, R. T. J., Bostock, M. G., & Christensen, N. I. (2012). Nature of the low velocity zone in Cascadia from receiver function waveform inversion. *Earth and Planetary Science Letters*, *337–338*, 25–38. https://doi.org/10.1016/j.epsl.2012.05.031

Hayes, G. P., & Furlong, K. P. (2007). Abrupt changes in crustal structure beneath the Coast Ranges of northern California-developing new techniques in receiver function analysis. *Geophysical Journal International*, *170*(1), 313–336. https://doi.org/10.1111/j.1365-246x.2007.03401.x

Hayes, G. P., Moore, G. L., Portner, D. E., Hearne, M., Flamme, H., Furtney, M., & Smoczyk, G. M. (2018). Slab2, a comprehensive subduction zone geometry model. *Science*, *362*(6410), 58–61. https://doi.org/10.1126/science.aat4723

Huot, G., & Singh, S. C. (2018). Seismic evidence for fluid/gas beneath the Mentawai Fore-Arc Basin, central Sumatra. *Journal of Geophysical Research: Solid Earth*, *123*(2), 957–976. https://doi.org/10.1002/2017JB014849

Jacob, J., Dyment, J., & Yatheesh, V. (2014). Revisiting the structure, age, and evolution of the Wharton Basin to better understand subduction under Indonesia. *Journal of Geophysical Research: Solid Earth*, *119*(1), 169–190. https://doi.org/10.1002/2013JB010285

Julià, J. (2007). Constraining velocity and density contrasts across the crust-mantle boundary with receiver function amplitudes. *Geophysical Journal International*, *171*(1), 286–301. https://doi.org/10.1111/j.1365-2966.2007.03502.x
Kawakatsu, H., Kumar, P., Takei, Y., Shinohara, M., Kanazawa, T., Araki, E., & Suyehiro, K. (2009). Seismic evidence for sharp lithosphere-asthenosphere boundaries of oceanic plates. *Science*, *324*(5926), 499–502. https://doi.org/10.1126/science.1169499
Kawakatsu, H., & Watada, S. (2007). Seismic evidence for deep-water transportation in the mantle. *Science*, *316*(5830), 1468–1471. https://doi.org/10.1126/science.1140855
Kennett, B. L. N., & Engdahl, E. R. (1991). Traveltimes for global earthquake location and phase identification. *Geophysical Journal International*, *105*(2), 429–465. https://doi.org/10.1111/j.1365-246X.1991.tb06724.x
Kennett, B. L. N., Engdahl, E. R., & Buland, R. (1995). Constraints on seismic velocities in the Earth from traveltimes. *Geophysical Journal International*, *122*(1), 108–124. https://doi.org/10.1111/j.1365-246X.1995.tb03540.x
Kikuchi, M., & Kanamori, H. (1992). Inversion of complex body waves. *Bulletin of the Seismological Society of America*, *72*(2), 491–506.
Kim, H. J., Kawakatsu, H., Akuhara, T., Shinohara, M., Shiobara, H., Sugioka, H., & Takagi, R. (2021). Receiver function imaging of the amphibious NE Japan subduction zone—Effects of low-velocity sediment layer. *Journal of Geophysical Research: Solid Earth*, *126*(9), 1–15. https://doi.org/10.1029/2021JB021918
Koulakov, I., Kasatkina, E., Shapiro, N. M., Jaupart, C., Vasilevsky, A., El Khrepy, S., et al. (2016). The feeder system of the Toba supervolcano from the slab to the shallow reservoir. *Nature Communications*, *7*, 1–12. https://doi.org/10.1038/ncomms12228
Laske, G., Masters, G., Ma, Z., & Pasyanos, M. E. (2012). CRUST1.0: An updated global model of earth's crust. *Geophysical Research Abstracts EGU General Assembly*, *14*, 2012–3743.
Levin, V., & Park, J. (1997). P-SH conversions in a flat-layered medium with anisotropy of arbitrary orientation. *Geophysical Journal International*, *131*(2), 253–266. https://doi.org/10.1111/j.1365-246X.1997.tb01220.x
Li, J., Song, X., Wang, P., & Zhu, L. (2019). A generalized H-κ method with harmonic corrections on Ps and its crustal multiples in receiver functions. *Journal of Geophysical Research: Solid Earth*, *124*(4), 3782–3801. https://doi.org/10.1029/2018JB016356
Li, X., Sobolev, S. V., Kind, R., Yuan, X., & Estabrook, C. (2000). A detailed receiver function image of the upper mantle discontinuities in the Japan subduction zone. *Earth and Planetary Science Letters*, *183*(3–4), 527–541. https://doi.org/10.1016/S0012-821X(00)00294-6
Ligorría, J. P., & Ammon, C. J. (1999). Iterative deconvolution and receiver-function estimation. *Bulletin of the Seismological Society of America*, *89*(5), 1395–1400. https://doi.org/10.1785/bssa0890051395
Liu, H., & Niu, F. (2012). Estimating crustal seismic anisotropy with a joint analysis of radial and transverse receiver function data. *Geophysical Journal International*, *188*(1), 144–164. https://doi.org/10.1111/j.1365-246x.2011.05249.x
Liu, S., Suardi, I., Xu, X., Yang, S., & Tong, P. (2021). The geometry of the subducted slab beneath Sumatra revealed by regional and teleseismic traveltime tomography. *Journal of Geophysical Research: Solid Earth*, *126*(1), 1–29. https://doi.org/10.1029/2020JB020169
Liu, S., Suardi, I., Zheng, M., Yang, D., Huang, X., & Tong, P. (2019). Slab morphology beneath northern Sumatra revealed by regional and teleseismic traveltime tomography. *Journal of Geophysical Research: Solid Earth*, *124*(10), 10544–10564. https://doi.org/10.1029/2019JB017625
McCaffrey, R. (2009). The tectonic framework of the Sumatran subduction zone. *Annual Review of Earth and Planetary Sciences*, *37*(1), 345–366. https://doi.org/10.1146/annurev.earth.031208.100212
Mukti, M. M. R., Singh, S. C., Deighton, I., Hananto, N. D., Moeremans, R., & Permana, H. (2012). Structural evolution of backthrusting in the Mentawai Fault Zone, offshore Sumatran forearc. *Geochemistry, Geophysics, Geosystems*, *13*(12), 1–21. https://doi.org/10.1029/2012GC004199
Nedimović, M. R., Hyndman, R. D., Ramachandran, K., & Spence, G. D. (2003). Reflection signature of seismic and aseismic slip on the northern Cascadia subduction interface. *Nature*, *424*(6947), 416–420. https://doi.org/10.1038/nature01840
Pesicek, J. D., Thurber, C. H., Widiyantoro, S., Engdahl, E. R., & Deshon, H. R. (2008). Complex slab subduction beneath northern Sumatra. *Geophysical Research Letters*, *35*(20), 1–5. https://doi.org/10.1029/2008GL035262
Piana Agostinetti, N., & Miller, M. S. (2014). The fate of the downgoing oceanic plate: Insight from the Northern Cascadia subduction zone. *Earth and Planetary Science Letters*, *408*, 237–251. https://doi.org/10.1016/j.epsl.2014.10.016
Porter, R., Zandt, G., & McQuarrie, N. (2011). Pervasive lower-crustal seismic anisotropy in Southern California: Evidence for underplated schists and active tectonics. *Lithosphere*, *3*(3), 201–220. https://doi.org/10.1130/l126.1
Qin, Y., & Singh, S. C. (2015). Seismic evidence of a two-layer lithospheric deformation in the Indian Ocean. *Nature Communications*, *6*, 1–12. https://doi.org/10.1038/ncomms9298
Qin, Y., & Singh, S. C. (2018). Insight into frontal seismogenic zone in the Mentawai locked region from seismic full waveform inversion of ultralong offset streamer data. *Geochemistry, Geophysics, Geosystems*, *19*(11), 4342–4365. https://doi.org/10.1029/2018GC007787
Rossi, G., Abers, G. A., Rondenay, S., & Christensen, D. H. (2006). Unusual mantle Poisson's ratio, subduction, and crustal structure in central Alaska. *Journal of Geophysical Research: Solid Earth*, *111*(B9), B09311. https://doi.org/10.1029/2005jb003956
Rost, S., & Thomas, C. (2002). Array seismology: Methods and applications. *Reviews of Geophysics*, *40*(3), 2-1–2–27. https://doi.org/10.1029/2000RG000100
Savage, M. K. (1998). Lower crustal anisotropy or dipping boundaries? Effects on receiver functions and a case study in New Zealand. *Journal of Geophysical Research: Solid Earth*, *103*(7), 15069–15087. https://doi.org/10.1029/98jb00795
Schneider, F. M., Yuan, X., Schurr, B., Mechie, J., Sippl, C., Haberland, C., et al. (2013). Seismic imaging of subducting continental lower crust beneath the Pamir. *Earth and Planetary Science Letters*, *375*, 101–112. https://doi.org/10.1016/j.epsl.2013.05.015
Schulte-Pelkum, V., & Mahan, K. H. (2014). A method for mapping crustal deformation and anisotropy with receiver functions and first results from USArray. *Earth and Planetary Science Letters*, *402*, 221–233. https://doi.org/10.1016/j.epsl.2014.01.050
Shiomi, K., & Park, J. (2008). Structural features of the subducting slab beneath the Kii Peninsula, central Japan: Seismic evidence of slab segmentation, dehydration, and anisotropy. *Journal of Geophysical Research: Solid Earth*, *113*(B10), B10318. https://doi.org/10.1029/2007jb005535
Shiomi, K., Sato, H., Obara, K., & Ohtake, M. (2004). Configuration of subducting Philippine Sea plate beneath southwest Japan revealed from receiver function analysis based on the multivariate autoregressive model. *Journal of Geophysical Research: Solid Earth*, *109*(4), 1–13. https://doi.org/10.1029/2003JB002774
Singh, S. C., Carton, H., Chauhan, A. S., Androvandi, S., Davaille, A., Dyment, J., et al. (2011). Extremely thin crust in the Indian Ocean possibly resulting from Plume-Ridge Interaction. *Geophysical Journal International*, *184*(1), 29–42. https://doi.org/10.1111/j.1365-246X.2010.04823.x
Singh, S. C., Carton, H., Tapponnier, P., Hananto, N. D., Chauhan, A. P. S., Hartoyo, D., et al. (2008). Seismic evidence for broken oceanic crust in the 2004 Sumatra earthquake epicentral region. *Nature Geoscience*, *1*(11), 777–781. https://doi.org/10.1038/ngeo336
Singh, S. C., Chauhan, A. P. S., Calvert, A. J., Hananto, N. D., Ghosal, D., Rai, A., & Carton, H. (2012). Seismic evidence of bending and unbending of subducting oceanic crust and the presence of mantle megathrust in the 2004 Great Sumatra earthquake rupture zone. *Earth and Planetary Science Letters*, *321–322*, 166–176. https://doi.org/10.1016/j.epsl.2012.01.012
Singh, S. C., Hananto, N. D., & Chauhan, A. P. S. (2011). Enhanced reflectivity of backthrusts in the recent great Sumatran earthquake rupture zones. *Geophysical Research Letters*, *38*(4), 1–5. https://doi.org/10.1029/2010GL046227

Singh, S. C., Hananto, N., Mukti, M., Robinson, D. P., Das, S., Chauhan, A., et al. (2011). Aseismic zone and earthquake segmentation associated with a deep subducted seamount in Sumatra. *Nature Geoscience*, *4*(5), 308–311. https://doi.org/10.1038/ngeo1119

Tan, P., Chen, Y., Sun, W., Li, W., Tang, G., & Cui, T. (2018). An improved H-κ-θ stacking method to determine the crustal thickness and bulk vP/vS ratios in the case of a slant Moho interface. *Chinese Journal of Geophysics*, *61*(9), 3689–3700. https://doi.org/10.6038/cjg2018M0032

Tang, G., Barton, P. J., McNeill, L. C., Henstock, T. J., Tilmann, F., Dean, S. M., et al. (2013). 3-D active source tomography around Simeulue Island offshore Sumatra: Thick crustal zone responsible for earthquake segment boundary. *Geophysical Research Letters*, *40*(1), 48–53. https://doi.org/10.1029/2012GL054148

Tauzin, B., Bodin, T., Debayle, E., Perrillat, J. P., & Reynard, B. (2016). Multi-mode conversion imaging of the subducted Gorda and Juan de Fuca plates below the North American continent. *Earth and Planetary Science Letters*, *440*, 135–146. https://doi.org/10.1016/j.epsl.2016.01.036

Tauzin, B., Reynard, B., Perrillat, J. P., Debayle, E., & Bodin, T. (2017). Deep crustal fracture zones control fluid escape and the seismic cycle in the Cascadia subduction zone. *Earth and Planetary Science Letters*, *460*, 1–11. https://doi.org/10.1016/j.epsl.2016.12.007

Tonegawa, T., Hirahara, K., Shibutani, T., & Fujii, N. (2006). Lower slab boundary in the Japan subduction zone. *Earth and Planetary Science Letters*, *247*(1–2), 101–107. https://doi.org/10.1016/j.epsl.2006.04.036

Wang, P., Wang, L., Mi, N., Liu, J., Li, H., Yu, D., et al. (2010). Crustal thickness and average Vp/Vs ratio variations in southwest Yunnan, China, from teleseismic receiver functions. *Journal of Geophysical Research: Solid Earth*, *115*(11), 1–13. https://doi.org/10.1029/2009JB006651

Wang, X., Bradley, K., Wang, X., Edward, K., Wei, S., & Wu, W. (2018). Active backstop faults in the Mentawai region of Sumatra, Indonesia, revealed by teleseismic broadband waveform modeling Active backstop faults in the Mentawai region of Sumatra, Indonesia, revealed by teleseismic broadband waveform modeling. *Earth and Planetary Science Letters*, *483*, 29–38. https://doi.org/10.1016/j.epsl.2017.11.049

Ward, K. M., Lin, F., & Schmandt, B. (2018). High-resolution receiver function imaging across the Cascadia subduction zone using a dense nodal array. *Geophysical Research Letters*, *45*(22), 12218–12225. https://doi.org/10.1029/2018GL079903

Wessel, P., & Smith, W. H. (1998). New, improved version of generic mapping tools released. *Eos, Transactions American Geophysical Union*, *79*(47), 579. https://doi.org/10.1029/98eo00426

Weston, J., Engdahl, E. R., Harris, J., Di Giacomo, D., & Storchak, D. A. (2018). ISC-EHB: Reconstruction of a robust earthquake data set. *Geophysical Journal International*, *214*(1), 474–484. https://doi.org/10.1093/gji/ggy155

Wirth, E. A., & Long, M. D. (2012). Multiple layers of seismic anisotropy and a low-velocity region in the mantle wedge beneath Japan: Evidence from teleseismic receiver functions. *Geochemistry, Geophysics, Geosystems*, *13*(8), Q08005. https://doi.org/10.1029/2012GC004180

Wu, C., Tian, X., Xu, T., Liang, X., Chen, Y., Taylor, M., et al. (2019). Deformation of crust and upper mantle in central Tibet caused by the northward subduction and slab tearing of the Indian lithosphere: New evidence based on shear wave splitting measurements. *Earth and Planetary Science Letters*, *514*, 75–83. https://doi.org/10.1016/j.epsl.2019.02.037

Yu, Y., Song, J., Liu, K. H., & Gao, S. S. (2015). Determining crustal structure beneath seismic stations overlying a low-velocity sedimentary layer using receiver functions. *Journal of Geophysical Research: Solid Earth*, *120*(5), 3208–3218. https://doi.org/10.1002/2014JB011610

Yuan, X., Sobolev, S. V., Kind, R., Oncken, O., Bock, G., Asch, G., et al. (2000). Subduction and collision processes in the Central Andes constrained by converted seismic phases. *Nature*, *408*(6815), 958–961. https://doi.org/10.1038/35050073

Zhang, J., Chen, L., & Wang, X. (2019). Crustal structure study based on principal component analysis of receiver functions. *Science China Earth Sciences*, *62*(7), 1110–1124. https://doi.org/10.1007/s11430-018-9341-9

Zhao, D., Fujisawa, M., & Toyokuni, G. (2017). Tomography of the subducting Pacific slab and the 2015 Bonin deepest earthquake (Mw 7.9). *Scientific Reports*, *7*(1), 1–8. https://doi.org/10.1038/srep44487

Zhao, D., Wang, J., Huang, Z., & Liu, X. (2021). Seismic structure and subduction dynamics of the western Japan arc Tectonophysics Seismic structure and subduction dynamics of the western Japan arc. *Tectonophysics*, *802*, 228743. https://doi.org/10.1016/j.tecto.2021.228743

Zhu, L., & Kanamori, H. (2000). Moho depth variation in southern California from teleseismic receiver functions. *Journal of Geophysical Research: Solid Earth*, *105*(B2), 2969–2980. https://doi.org/10.1029/1999JB900322

References From the Supporting Information

Boness, N. L., & Zoback, M. D. (2006). Mapping stress and structurally controlled crustal shear velocity anisotropy in California. *Geology*, *34*(10), 825–828. https://doi.org/10.1130/G22309.1

Brownlee, S. J., Schulte-Pelkum, V., Raju, A., Mahan, K., Condit, C., & Orlandini, O. F. (2017). Characteristics of deep crustal seismic anisotropy from a compilation of rock elasticity tensors and their expression in receiver functions. *Tectonics*, *36*(9), 1835–1857. https://doi.org/10.1002/2017tc004625

Collings, R., Rietbrock, A., Lange, D., Tilmann, F., Nippress, S., & Natawidjaja, D. (2013). Seismic anisotropy in the Sumatra subduction zone. *Journal of Geophysical Research: Solid Earth*, *118*(10), 5372–5390. https://doi.org/10.1002/jgrb.50157

Dziewonski, A. M., & Anderson, D. L. (1981). Preliminary reference Earth model. *Physics of the Earth and Planetary Interiors*, *25*(4), 297–356. https://doi.org/10.1016/0031-9201(81)90046-7

Hammond, J. O. S., Wookey, J., Kaneshima, S., Inoue, H., Yamashina, T., & Harjadi, P. (2010). Systematic variation in anisotropy beneath the mantle wedge in the Java-Sumatra subduction system from shear-wave splitting. *Physics of the Earth and Planetary Interiors*, *178*(3–4), 189–201. https://doi.org/10.1016/j.pepi.2009.10.003

Horen, H., Zamora, M., & Dubuisson, G. (1996). Seismic waves velocities and anisotropy in serpentinized peridotites from Xigaze ophiolite: Abundance of serpentine in slow spreading ridge. *Geophysical Research Letters*, *23*(1), 9–12. https://doi.org/10.1029/95gl03594

Katayama, I., Hirauchi, K. I., Michibayashi, K., & Ando, J. I. (2009). Trench-parallel anisotropy produced by serpentine deformation in the hydrated mantle wedge. *Nature*, *461*(7267), 1114–1117. https://doi.org/10.1038/nature08513

Long, M. D., & Silver, P. G. (2008). The subduction zone flow field from seismic anisotropy: A global view. *Science*, *319*(5861), 315–318. https://doi.org/10.1126/science.1150809

Nagaya, M., Oda, H., Akazawa, H., & Ishise, M. (2008). Receiver functions of seismic waves in layered anisotropic media: Application to the estimate of seismic anisotropy. *Bulletin of the Seismological Society of America*, *98*(6), 2990–3006. https://doi.org/10.1785/0120080130

Niu, F., & Li, J. (2011). Component azimuths of the CEArray stations estimated from P-wave particle motion. *Earthquake Science*, *24*(1), 3–13. https://doi.org/10.1007/s11589-011-0764-8

Reynard, B. (2013). Serpentine in active subduction zones. *Lithos*, *178*, 171–185. https://doi.org/10.1016/j.lithos.2012.10.012

Savage, M. K. (1999). Seismic anisotropy and mantle deformation: What have we learned from shear wave splitting? *Reviews of Geophysics*, *37*(1), 65–106. https://doi.org/10.1029/98rg02075

Wang, X., Chen, Q., Li, J., & Wei, S. (2016). Seismic sensor misorientation measurement using P-wave particle motion: An application to the NECsaids array. *Seismological Research Letters*, *87*(4), 1–11. https://doi.org/10.1785/0220160005